IEEE Access
Multidisciplinary | Rapid Review | Open Access Journal

IEEE MAGNETICS SOCIETY SECTION

Received 16 January 2023, accepted 15 February 2023, date of publication 23 February 2023, date of current version 1 March 2023.

Digital Object Identifier 10.1109/ACCESS.2023.3248290

RESEARCH ARTICLE

Simulation of a Transverse Flux Linear Induction Motor to Determine an Equivalent Circuit Using 3D Finite Element

JUAN ANTONIO DOMÍNGUEZ HERNÁNDEZ[1], NATIVIDAD DURO CARRALERO[1], AND ELENA GAUDIOSO VÁZQUEZ[2]

[1]Departamento de Informática y Automática, ETSI Informática, Universidad Nacional de Educación a Distancia (UNED), 28040 Madrid, Spain
[2]Departamento de Inteligencia Artificial, ETSI Informática, Universidad Nacional de Educación a Distancia (UNED), 28040 Madrid, Spain

Corresponding author: Juan Antonio Domínguez Hernández (juanantoniodguez83@gmail.com)

This work was supported in part by the Spanish Ministry of Science and Innovation under Project PID2019-108377RB-C32, and in part by the Universidad Nacional de Educación a Distancia under Grant GID2016-6.

ABSTRACT This paper presents a Transverse Flux Linear Induction Motor prototype simulated with a 3D Finite Element tool. The main objective of the paper is to obtain an accurate method to construct an equivalent circuit that simulates the motor, using some specific parameters. The method has three steps. In the first step, we simulate two indirect tests to represent rotating induction machines, standstill and locked rotor tests. Using the test results, we define an equations system that incorporates the longitudinal end-effect. The system allows us to select specific parameters needed to build the equivalent circuit using six different configurations. In the second step, we classify the parameters in two groups: parameters from the primary and secondary parts. We test the primary part parameters defining the magnetizing inductance as a combination of the longitudinal and the transversal magnetizing inductance. To this end, the method analyses the first harmonic of the magnetic field wave along the air gap, which is located above the central teeth. Thus, it is possible to establish a difference between transversal and longitudinal components of the magnetic field density. The parameters of the secondary part will be compared using 2D Field Theory with a linear induction motor that operates with a transverse flux configuration. In the third step, the method analyses the selected parameters using a goodness factor, a dimensionless key performance indicator, specifically used to evaluate the behavior of linear induction motors and the specific parameters estimated for the equivalent circuit.

INDEX TERMS Air gap magnetic flux density, equivalent circuit, goodness factor, indirect tests, magnetizing inductance, transverse flux linear induction motor.

I. INTRODUCTION

A linear Induction Motor (LIM) is a special motor that allows a linear motion. It is different from traditional rotating induction motors (RIM), most usually used [1]. A LIM is composed of two different parts. The primary part is oriented to the coils allocation that conforms the machine winding and the secondary part is made of several layers of materials with different magnetic and electrical properties, like aluminium or steel. Fig. 1 shows a LIM. We can see the primary part, whose coils generate the travelling magnetic field and the main electromagnetic forces inside the LIM [2] and the separation between both parts. In this region, electromagnetic conversion is created. A LIM has two operation modes: Linear Electric Actuator (LEA), when linear motor produces electric forces and Linear Electric Generator (LEG), when motor converts mechanical power into alternate current (AC) electric power [3].

The impact of LIMs in the industry is huge, because there are many military and civil applications. For example, LEAs are used for positioning on computer peripherals or in high-thrust-density conditions, such as aircraft engines or modern transportation systems for urban and interurban purposes. The absence of mechanical transmission between fixed and

The associate editor coordinating the review of this manuscript and approving it for publication was Montserrat Rivas.

This work is licensed under a Creative Commons Attribution-NonCommercial-NoDerivatives 4.0 License.
For more information, see https://creativecommons.org/licenses/by-nc-nd/4.0/

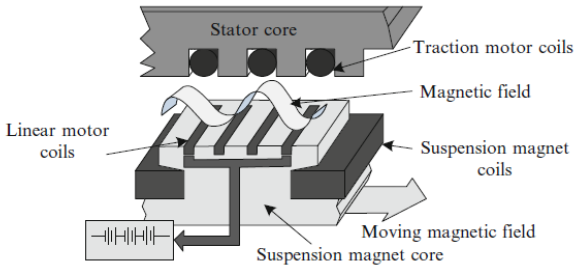

FIGURE 1. View of a linear induction motor adapted from [2].

moving parts allows the design of vehicles powered by linear motors, reducing dead weight and energy consumption with respect to the RIM. LIMs can also operate as linear pumps in hydrodynamic applications, where the movement of liquid metal is necessary. In the case of LEGs, through a configuration of a tubular alternator, they can be combined with motors to also generate electricity [3], [4].

LIMs can be classified according to two criteria. The first considers some geometric aspects and the number of available primary parts and determines two types of machines. A Single Sided Linear Induction Motor (SSLIM) when only operates a winding motor in the machine and a Double-Sided Linear Induction Motor (DSLIM) when two are operating. The second criterion classifies LIMs attending to the configuration of the magnetic flux. If the magnetic flux moves along the direction of the motion, it is called Longitudinal Flux Linear Induction Motor (LFLIM) and when the magnetic flux moves along a plane normal to the direction of the motion, it is called Transverse Induction Motor (TFLIM). The main advantage of TFLIM is the less restrictive requirements on the magnetizing current consumed compared to the longitudinal flux. TFLIM has also less core weight than a LIM, so it has large pole pitches [5]. For these reasons, in this paper, we have decided to implement a TFLIM.

TFLIM control methods, equivalent circuit estimations and field analysis and design are now three active research areas. Therefore, novel computation techniques are applied in these areas to achieve accurate results. Finite Element Method (FEM) is an appropriate way to determine fundamental aspects involved in electrical machine engineering [6], because it allows calculating the distribution of magnetic and electric fields considering some geometrical aspects and the nonlinear characteristics of the materials used. Ferromagnetic materials, permanent magnets and conductor electrical specifications are the most common nonlinear behaviours that can be simulated with FEM tools [7], [8].

There are different papers in the literature focused on the estimation of equivalent circuit estimations [9], [10], [11]. In these papers, indirect tests are analysed but FEM is not used to estimate the equivalent circuit. Authors use real experimental tests to determine the electrical parameters associated with their linear electrical devices. The indirect used tests, no load and standstill, are discussed in the case of a longitudinal magnetic flux configuration. Therefore, indirect tests are a suitable way to consider the high air gap that a LIM has, where the secondary part is composed of a slotted construction. Consequently, leakage fluxes cannot be neglected because it would imply a decrease in efficiency. In this paper, we use indirect tests to estimate the parameters, but as a novelty, we use FEM-3D tools to determine the equivalent circuit.

In [12], [13], [14], and [15] analytical methods are used to measure some special effects that occur in LIMs but not in RIMs, which are very important to determine the equivalent circuit parameters. In [12] transverse edge effect is analysed considering several geometries linked to the aluminium layer, and in [13] the behaviour of a LIM with a ladder secondary structure is detailed. Although this special steel layer construction is not applied in our TFLIM, we reference this paper because the authors use FEM-3D and compare the results with an analytical model. In [14] some relevant coefficients are estimated, such as the saturation coefficient due to the steel layer and the skin effect inside the aluminium plate to evaluate the electric conductivity linked to the secondary part. In [15] authors also use FEM-3D to compare the transverse edge effect between various secondary cage configurations. Particularly, in [16] and [17] authors indicate the progressive relevance of TFLIM in the high-speed magnetic levitation transport system, where a mathematical model is used to describe the induced eddy currents. Finally, in [18] Transverse Flux Linear Motor with permanent-magnet excitation is also studied with FEM-2D techniques.

The LIM simulated in this paper is a single-sided topology with a transverse flux configuration. Our objective is to estimate the main parameters of an equivalent circuit (EC) per phase of the TFLIM using FEM-3D. We assume that any type of LIM, both transverse and longitudinal, can be analysed by taking as starting point the T-type equivalent circuit proposed for RIMs. This model of equivalent circuit is widely used with LIMs [19], [20], [21]. In [19] a classical T-type topology is adapted to new approaches to magnetizing inductance, including the slip effect of variations in the magnetic field density along the air gap. In [20] T-type circuit is modified from RIM to LIM to include some special effects. Finally, in [21] an equivalent model of π derived from RIMs, which includes the specific phenomena of a LIM.

This paper is focused on offline parameters identification, where indirect tests using FEM-3D will be simulated to obtain the main parameters of an equivalent circuit. In the first step of LIM design, we simulate the experimental tests using FEM-3D with a coupled electrical circuit, so that the frequencies can be modified. In addition, we estimate the main parameters of the LIM using electromagnetic field theory to verify the results obtained with the simulations.

The rest of the paper is organised as follows. Section II shows the main geometric and physical characteristics of the selected TFLIM and the details of the winding factor structure. Section III describes the steps followed to simulate indirect tests with FEM-3D. The general equations are also detailed, using statistical methods for the calculation

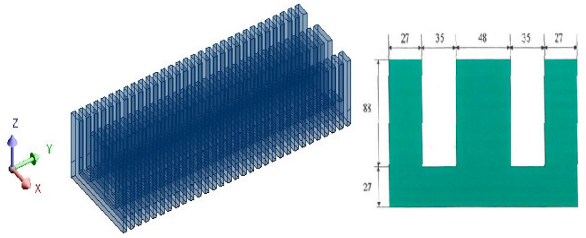

FIGURE 2. 3D-view of TFLIM primary part and dimension in mm of a ferromagnetic sheet [23], [24].

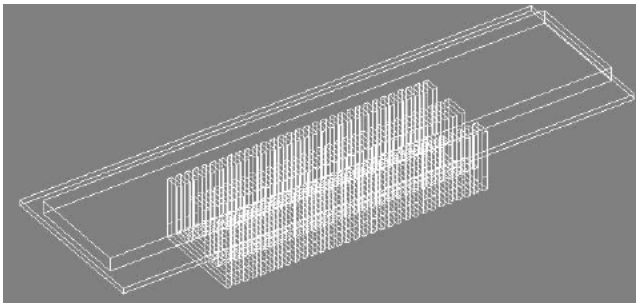

FIGURE 3. 3D-view of TFLIM built in FEM-3D tool [24].

of the parameters of the indirect tests, when the TFLIM works under a different range of frequencies. In section IV, we specify the equations system that allows us to estimate the parameters necessary for the equivalent circuit per phase corresponding to a T-type circuit model. To verify the results obtained, we propose in section V a method that calculates the magnetizing inductance taking as reference the value of the magnetic field density along the air gap. Furthermore, we use an alternative method based on 2D field theory, to obtain data from secondary part and compare them with values from the indirect tests. In addition, particular phenomena are also calculated in TFLIM such as the fringing effect, Carter's coefficient or skin effect, among others. In section VI, the quality of the TFLIM is evaluated using a goodness factor [22]. Finally, the main conclusions of the paper are presented.

II. DESCRIPTION OF THE TFLIM MODEL

In this section, the developed TFLIM topology is described. Firstly, the main geometric parameters involved are exposed [23]. Secondly, the materials used in the construction of this type of electric machine and the hypothesis assumed to simulate everything with FEM-3D are described. Finally, the main characteristics of the motor winding are detailed.

The proposed TFLIM was built in the 90s by the Spanish Polytechnic University of Madrid. This prototype was tested under standstill and low voltage level conditions, and the authors established some future works at simulating the TFLIM with FEM-3D tools to improve knowledge of the phenomena that occur in this type of LIM. The main use of the TFLIM discussed is for the construction of single-gilder transport railway systems, where TFLIM can be used to achieve thrust and levitation forces while decreasing the consumed power [23].

In [24], this model was simulated with FEM-3D tools to analyse the main forces developed in transient regime and several geometric configurations were also tested. Thus, the primary part of the motor is composed by 31 ferromagnetic sheets with an E-shape configuration, as it is shown in Fig. 2. Fig. 3 shows the secondary part composed by two layers, aluminium and steel, using FEM-3D tools. The mechanical air gap between primary and secondary part is set to 5 mm. The other dimensions and the material properties used in the simulations are presented in Table 1.

TABLE 1. Dimensions and properties in the TFLIM.

TFLIM Geometric Parameters [mm]					
Primary Part Dimension		**Secondary Part Dimension**			
Width Longitudinal Slot	8.5	**Aluminium Layer**		**Steel Layer**	
Slot Pitch	16.5	Thickness Aluminium	10	Thickness Steel	25
Primary Part Length	503.5	Width Aluminium	300	Width Steel	195
Pole pitch	200	Length Aluminium	990	Length Steel	970
Mechanical Air gap					5
Material Properties used in FEM 3-D					
Electrical/magnetic quantities		**Aluminium**	**Steel**	**Cooper**	
Conductivity/Resistivity		$3.73 \cdot 10^7$ S/m	0	$2.37 \cdot 10^{-2}$	
Relative Permeability		1	2500	1	

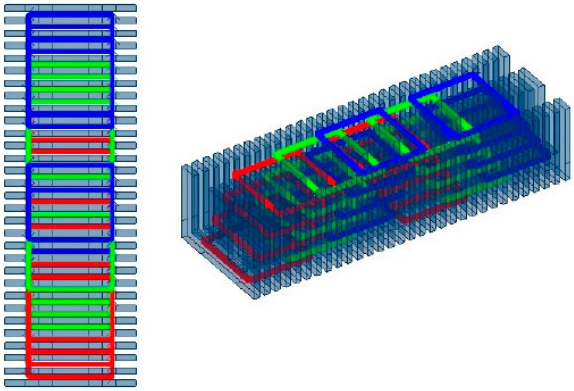

FIGURE 4. 3D view of TFLIM winding and location of coils by each phase [24].

A. TFLIM WINDING FACTOR STRUCTURE

This section presents the main properties of the winding used to measure the winding factor. Fig. 4 shows the coils that have been designed using FEM-3D. A three-phase winding is located inside armature of the primary part. Phase A coils are represented in red, phase B coils in blue and phase C coils in green.

The TFLIM has a double layer winding, so coils are located at the top and bottom. However, due to graphical restrictions, they are represented by four layers.

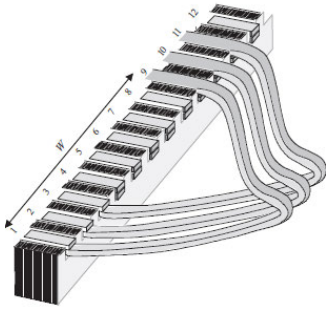

FIGURE 5. Representation of slots spans by a generic coil in a double-layer winding [25].

TABLE 2. TFLIM winding parameters.

Characteristic Parameters from TFLIM winding						
Q	y_Q	W	τ_P	K_{d1}	K_{p1}	K_{w1}
24	4	6	12	0.958	0.707	0.6773

To determine the winding factor, it must be established the difference between $\mathcal{Q}$, which denotes the number of slots in the primary part, and y_Q, which represents the number of slots per pole and phase [25]. Equation (1) calculates y_Q where $\mathcal{Q} = 24$, $m = 3$, is the number of phases and $p = 1$ is the number of pole pairs.

$$y_Q = {\mathcal{Q}}/{(2 \cdot m \cdot p)} \tag{1}$$

Next, the winding factor K_{w1} must be estimated, which is calculated by the product between the distribution factor, K_{d1} and the pitch factor K_{p1}, according to the Eq. (2), (3) and (4). For more details, see reference [25].

$$K_{w1} = K_{d1} \cdot K_{p1} \tag{2}$$

$$K_{d1} = sin\left(\tfrac{\pi}{2 \cdot m}\right) \Big/ \left(q \cdot sin \cdot \left({\pi}/{2 \cdot m \cdot q}\right)\right) \tag{3}$$

$$K_{p1} = sin\left({W}/{\tau_P} \cdot {\pi}/{2}\right) \tag{4}$$

These equations consider only the first harmonic in the magnetic field density created by the primary winding. In these equations the parameter $W = 6$ is involved, which represents the width of a single coil whose dimension is less than the pole pitch τ_P. Both, W and τ_P are expressed by the number of slots as it is shown in Fig. 5. Table 2 shows the values of TFLIM winding factors used in this paper. The winding factor is around 0.67 and K_{d1} and K_{p1} around 0.96 and 0.7 respectively.

III. FEM-3D SIMULATIONS

In this section, we are going to explain the main features of the simulations using FEM-3D. Subsection III-A describes the necessary conditions to simulate the TFLIM with FEM-3D using a coupled circuit to supply the motor. Subsection III-B explains the indirect tests used: blocked secondary test and no load test. The first one estimates total impedance of the TFLIM and the second is oriented to decouple the effect linked to the secondary part from the equivalent circuit to calculate the primary part parameters.

A. SIMULATION CONDITIONS, HYPOTHESIS AND SIMPLIFICATIONS

A Y-connected three phase equilibrated voltage system operates according to equations (5) to (7). In [24] the process to determine V_{LINE} is described, which is the peak value of the voltage sources. $V_{LINE} = 660V$ is the voltage level necessary to correctly magnetize a TFLIM. The maximum value of the magnetic field density along the air gap reaches a peak value around 0.8 T. V_{Phase_a} [V], V_{Phase_b}[V] and V_{Phase_c}[V] are the instantaneous values of the source voltage linked to each phase, ω [rad/s] is the angular frequency, f [Hz] is the nominal supply frequency and t [s] is the instantaneous value of the simulation time [24].

$$\begin{aligned} V_{Phase_a}(t) &= V_{LINE} \cdot {\sqrt{2}}\Big/{\sqrt{3}} \cdot \cos(\omega \cdot t) \\ &= V_{LINE} \cdot {\sqrt{2}}\Big/{\sqrt{3}} \cdot \cos(2 \cdot \pi \cdot f \cdot t)) \end{aligned} \tag{5}$$

$$\begin{aligned} V_{Phase_b}(t) &= V_{LINE} \cdot {\sqrt{2}}\Big/{\sqrt{3}} \cdot \cos\left(\omega \cdot t - {2 \cdot \pi}/{3}\right) \\ &= V_{LINE} \cdot {\sqrt{2}}\Big/{\sqrt{3}} \cdot \cos\left(2 \cdot \pi \cdot f \cdot t - {2 \cdot \pi}/{3}\right) \end{aligned} \tag{6}$$

$$\begin{aligned} V_{Phase_c}(t) &= V_{LINE} \cdot {\sqrt{2}}\Big/{\sqrt{3}} \cdot \cos\left(\omega \cdot t + {2 \cdot \pi}/{3}\right) \\ &= V_{LINE} \cdot {\sqrt{2}}\Big/{\sqrt{3}} \cdot \cos\left(2 \cdot \pi \cdot f \cdot t + {2 \cdot \pi}/{3}\right) \end{aligned} \tag{7}$$

To simulate the TFLIM in FEM 3-D the next hypothesis and simplifications are considered:

1. Linear B-H curve from ferromagnetic materials is described by a straight line with a relative permeability equal to 2500 (see Table 1). Therefore, the steel in primary part and the iron layer in secondary part operate under no saturation conditions, and therefore, iron losses can be neglected.
2. The effect of lamination effect to reduce eddy currents within ferromagnetic materials is not considered. Staking factor is equal to 1, which implies a great saving in the calculation effort. Therefore, it is not necessary to design insulating regions to reduce the non-desired effect linked to Foucault's currents [26].
3. According to Table 2 our work does not include the variation of electric resistivity-conductivity when the temperature increases. The heat conditions are uniform, so the electric conductivity during the simulations cannot fluctuate. Also, the electric conductivity inside the iron layer is equal to zero, so eddy currents will only be induced inside the aluminium layer. Therefore, the linear electrical

TABLE 3. Electric parameters from the EC of a LIM.

TFLIM Electric Parameters	
$\mathbf{L_m}$	Magnetizing Inductance [H].
$\mathbf{L_{ls}}$	Leakage primary inductance [H]
$\mathbf{L_s}$	Primary inductance [H].
$\mathbf{L_{lr}}$	Leakage secondary inductance [H].
$\mathbf{L_r}$	Secondary inductance [H].
$\mathbf{R_r}$	Secondary resistance [Ω].

resistivity in aluminium layer and copper used in coils belong to the primary winding.

4. Longitudinal end effect (LEE) is not included within the equivalent circuit, as it produces non-uniform velocity, unbalanced phase current and parasitical braking forces. Generally, this phenomenon is included within the parallel magnetizing branch of the equivalent circuit through an impedance that decreases the efficiency of the LIM [4].

B. INDIRECT TESTS IN A TFLIM USING FEM-3D

Two indirect tests are developed to obtain the main electrical parameters of the EC. Classic laboratory experiments are replicated to obtain the EC of our TFLIM [10], [19], [27], [28]. Using FEM-3D, the designer can save unnecessary prototypes constructions to determine the circuit. Two indirect tests have been simulated: the blocked secondary test and the no load test. From the blocked secondary test, the total impedance per phase of the TFLIM has been obtained and from the no load test, we can obtain the total inductance belonging to the primary part. The results of the both tests have been entered into a system of equations to identify the EC parameters shown in Table 3.

1) BLOCKED SECONDARY TEST

Blocked secondary test operates under standstill conditions where the secondary part has a linear velocity equal to 0 m/s. It is equivalent to a slip equal to 1, according to Eq. (8). It represents the difference between the synchronous velocity related to the magnetic field density of the primary part, $\boldsymbol{v_s}[m/s]$ and $\boldsymbol{v_{moving_part}}[m/s]$, that is the velocity of the secondary part. Synchronous velocity, $\boldsymbol{v_s}$, is given by Eq. (9), where $\tau_p[mm]$ is the pole pitch of the TFLIM set at 200 mm. and $f_{supply}[Hz]$ is the frequency of the sinusoidal voltage source whose variation depends on the simulation conditions. The results of the blocked secondary tests are used to estimate the parameters $\mathbf{L_{eq}}$ [H] (equivalent inductance) and $\mathbf{R_{eq}}$ [Ω] (equivalent resistance) of our TFLIM.

$$s = {v_s - v_{moving_part}}/{v_s} \tag{8}$$

$$v_s = 2 \cdot \tau_p \cdot f_{supply} \tag{9}$$

TABLE 4. Set-up of characteristic times for blocked secondary part tests in FEM-3D.

Main times for simulating blocked tests in FEM-3D			
$\mathbf{f_{supply}}$ [Hz]	$\mathbf{T_{cycle}}$ [ms]	$\mathbf{T_{simulation}}$ [ms]	$\mathbf{T_{sample}}$ [ms]
55	18.182	54.545	1.818
60	16.667	50.000	1.667
70	14.286	42.857	1.429
80	12.500	37.500	1.250
90	11.111	33.333	1.111
100	10.000	30.000	1.000

For this, it is necessary that a large electric current operates through the TFLIM. So, the EC circuit for this test is equal to a series circuit with equivalent inductance (L_{eq}) and equivalent resistance (R_{eq}) [27] representing the total inductance and resistance of the TFLIM. With these parameters, the value of the magnetizing inductance L_m and the secondary leakage inductance, L_{lr} are estimated.

The blocked tests have been designed using a frequency range of 55 Hz to 100 Hz, given by $\mathbf{f_{supply}}$ [Hz]. Table 4 shows the characteristic times set-up needed to reach the stationary state during the simulations. The first column shows the selected frequencies, second column the $\mathbf{T_{cycle}}$ [ms] (cycle time), that is, the period of the AC voltage source coupled to our TFLIM, third column corresponds to the $\mathbf{T_{simulation}}$ [ms] (simulation time) which is equal to the number of cycles to achieve a permanent regime in the simulations. And the last column shows $\mathbf{T_{sample}}$ [ms] (sample time) which is the portion of T_{cycle} needed to achieve a convergence solution. Eqs. (10), (11) and (12) are used to obtain these values.

$$T_{cycle} = {1}/{f_{supply}} \tag{10}$$

$$T_{sample} = {T_{cycle}}/{10} \tag{11}$$

$$T_{simulation} = 3 \cdot T_{cycle} \tag{12}$$

Once the TFLIM has been simulated in a transitory state according to the parameters of Table 4, an analytical method have been developed to calculate R_{eq} and L_{eq}. For this, it is important to remember that a TFLM is supplied through three-phase voltage sources, and that the frequency variation depends on the velocity of the TFLIM and on the voltage sources period. The analytical method has been developed in three steps:

1. Measurement of the active powers and electric currents for each phase in FEM-3D using an unbalanced system of electrical currents and active powers according to Eq. (13). Term 1 represents the absorbed active power of each voltage source ($P_{sh_a}[W]$, P_{sh_b}[W], $P_{sh_c}[W]$) and the

total active power consumed by the TFLIM ($P_{sh}[W]$). The 'sh' subscript indicates 'short-circuit' because the blocked test on a TFLIM corresponds to a short-circuit test. Term 2 shows the absorbed electrical currents of each phase (i_{sh_a}[A], i_{sh_b}[A], i_{sh_c}[A]) and the equivalent resistance per phase in the equivalent circuit ($R_{eq}[\Omega]$).

$$\underbrace{\sum_{i=1}^{3} P_{sh} = P_{sh_a} + P_{sh_b} + P_{sh_c}}_{Teram1} = \underbrace{\left(i_{sh_a}^2 + i_{sh_b}^2 + i_{sh_c}^2\right) \cdot R_{eq}}_{Term2} \quad (13)$$

2. Estimation of the power factors per phase $cos\gamma_{sh_a}$, $cos\gamma_{sh_b}$, and $cos\gamma_{sh_c}$. Equation (14) shows the relationship between the power factor with each active power per phase respectively, where $V_{LINE} = 660V$.

$$\begin{aligned} cos\gamma_{sh_a} &= {}^{P_{sh_a}}/_{V_{LINE} \cdot i_{sh_a}}, \\ cos\gamma_{sh_b} &= {}^{P_{sh_b}}/_{V_{LINE} \cdot i_{sh_b}}, \\ cos\gamma_{sh_c} &= {}^{P_{sh_c}}/_{V_{LINE} \cdot i_{sh_c}} \end{aligned} \quad (14)$$

3. Determination of the equivalent inductance, $L_{eq}[H]$. Equation (15) is used to estimate the total reactive power, $Q_{sh}[VAr]$.$Q_{sh_a}[VAr]$, $Q_{sh_b}[VAr]$ and $Q_{sh_c}[VAr]$ are the reactive powers per phase and $X_{eq}[\Omega]$ is the equivalent reactance. The relationship between X_{eq} and L_{eq} is given by Eq. (16), where $\omega_e[{}^{rad}/_{s}]$ is the source electrical angular frequency. Finally, L_{eq} is calculated by Eq. (17), combining Eqs. (15) and (16).

$$\underbrace{\sum_{i=1}^{3} Q_{sh} = Q_{sh_a} + Q_{sh_b} + Q_{sh_c}}_{Term1} = \underbrace{\left(i_{sh_a}^2 + i_{sh_b}^2 + i_{sh_c}^2\right) \cdot X_{eq}}_{Term2} \quad (15)$$

$$X_{eq} = \omega_e \cdot L_{eq} = 2 \cdot \pi \cdot f_{supply} \quad (16)$$

$$L_{eq} = \left(V_{LINE} \cdot \left(i_{sh_a} \cdot \sin\gamma_{sh_a} + i_{sh_b} \cdot \sin\gamma_{sh_b} + i_{sh_c} \cdot \sin\gamma_{sh_c}\right) \Big/ \left(i_{sh_a}^2 + i_{sh_b}^2 + i_{sh_c}^2\right)\right) \cdot \frac{1}{\omega_e} \quad (17)$$

2) NO LOAD TEST

The no load condition test, also called open-secondary circuit test, is used to estimate the primary part inductance, L_s. To simulate this test, the secondary part must be reduced [27]. This test has a slip equal to zero because the velocity of the moving part and the synchronous velocity are the same. So, to prepare the simulation with FEM-3D, two rules must be followed:

1. Connect the secondary part of the motor to a synchronous speed or to a slip equal to zero, that isolates the effect of the secondary circuit [27]. Without relative movements between the synchronous velocity linked to the magnetic field created by the primary part and the secondary part velocity, the variation of the magnetic flux is extremely low. Consequently, the induced eddy current inside the aluminium plate and the generated thrust force decrease. Furthermore, adding this effect with the assumption that the field harmonics can be negligible, there are no induced currents within the secondary part of the TFLIM.
2. Reduce the end effect of the TFLIM. For this, the TFLIM should operate under low frequencies [27]. For frequencies below 18 Hz, the effect due to the finite length of the TFLIM could be reduced considerably. Thus, Table 5 shows the selected frequencies to simulate the test with FEM-3D.

TABLE 5. Set-up of characteristic times for no load test.

Conditions to simulate the No load test				
f_{supply} [Hz]	T_{cycle} [ms]	$T_{simulation}$ [ms]	T_{sample} [ms]	V_{sec} [m/s]
18	55.556	166.667	5.556	7.2
16	62.500	187.500	6.250	6.4
14	71.429	214.286	7.143	5.6
12	83.333	250.000	8.333	4.8
10	100.000	300.000	10.000	4
8	125.000	375.000	12.500	3.2

Once the simulation has been prepared, to obtain $L_s[H]$, the developed method that simulates the no load test divided in three steps:

1. Calculation of the reactive power associated with each phase. Equations (18) and (19) estimate the value of L_s. In Term 1 $Q_{o_a}[VAr]$, $Q_{o_b}[VAr]$ and $Q_{o_c}[VAr]$ represent the reactive power in each phase and $Q_o[VAr]$ the total reactive power linked to the TFLIM. Term 2 shows the electrical currents, where $i_{o_a}[A]$, $i_{o_b}[A]$ and $i_{o_c}[A]$ are the absorbed values of each phase and $X_s[\Omega]$ the equivalent reactance. Then, the relationship between X_s and L_s is given by Eq. (19), where $\omega_e[{}^{rad}/_{s}]$ is the electrical angular frequency of the source.

$$\underbrace{\sum_{i=1}^{3} Q_o = Q_{o_a} + Q_{o_b} + Q_{o_c}}_{Term1} = \underbrace{\left(i_{O_a}^2 + i_{o_b}^2 + i_{O0c}^2\right) \cdot X_S}_{Term2} \quad (18)$$

$$X_s = \omega_e \cdot L_s = 2 \cdot \pi \cdot f_{supply} \quad (19)$$

2. Calculation of the electrical angle of each phase ($\gamma_{o_a}[^\circ]$, $\gamma_{o_b}[^\circ]$ and $\gamma_{o_c}[^\circ]$) between voltage sources and electric

currents of each phase using Eq. (20).

$$\sin\gamma_{o_a} = Q_{o_a}/V_{LINE}\cdot i_{o_a},$$
$$\sin\gamma_{o_b} = Q_{o_b}/V_{LINE}\cdot i_{o_b},$$
$$\sin\gamma_{o_c} = Q_{o_c}/V_{LINE}\cdot i_{o_c} \quad (20)$$

3. Combine the previous equations to obtain Eq. (21), which calculates $L_s[H]$:

$$L_s = \left(V_{LINE}\cdot\left(i_{o_a}\cdot\sin\gamma_{o_a}+i_{o_b}\cdot\sin\gamma_{o_b}+i_{o_c}\cdot\sin\gamma_{o_c}\right)\right/\left(i_{o_a}^2+i_{o_b}^2+i_{o_c}^2\right)\Big)\cdot\frac{1}{\omega_e} \quad (21)$$

3) ESTIMATION OF THE DIRECT CURRENT (DC) PRIMARY RESISTANCE

To achieve all the necessary EC parameters, the primary resistance must be estimated, R_s. This estimation is made analytically using Eq. (22) that uses the characteristics of the primary windings [23]. $\overline{L}_{coil}[mm]$ is the average length of a single coil that can be approximated to 526.5 mm, $\rho_{Cu}[\Omega\cdot mm^2/m]$ is the conductivity of the copper wire with a value of $2.37\cdot10^{-2}$, n_{phase} equals 8 (the number of coils per phase), $S_c\left[mm^2\right]$ is the cross-sectional area of the conductor equal to 1.7 and N_{phase} is the number of turns per phase, whose value is fixed at 22 turns. So, in our TFLIM the estimation of DC resistance per phase is 2.58Ω.

$$R_s = n_{phase}\cdot\left(\rho_{Cu}\cdot\overline{L}_{coil}\cdot N_{phase}\right)/S_c \quad (22)$$

IV. SYSTEM OF EQUATIONS

Once L_s, R_{eq}, L_{eq} and R_s are obtained through the indirect tests, a system of equations is implemented to determine the parameters of the equivalent circuit shown in Table 3. The system of equations is made up of following five equations ((23) to (27)).

$$R_{eq} = R_s + \frac{\omega_e^2\cdot L_m^2\cdot R_r}{R_r^2+\omega_e^2\cdot L_r^2} \quad (23)$$

$$L_{eq} = L_S - L_m + L_m\cdot\left[R_r^2+\omega_e^2\cdot L_r\cdot(L_r-L_m)\right]\Big/R_r^2+\omega_e^2\cdot L_r^2 \quad (24)$$

$$\beta = \frac{L_m}{L_r} \quad (25)$$

$$F_y = F_{y1} - F_{y2} = 3\cdot I_2^2\cdot R_r\cdot\frac{\pi}{\omega_2\cdot\tau_p} - \frac{3\cdot I_m^2\,(L_m+L_{lr})}{L} \quad (26)$$

$$I_s = I_m + I_2 \quad (27)$$

To generate the system necessary to calculate R_{eq} and X_{eq}, it is used an equivalent circuit under stationary state, where the values of R_{eq} and X_{eq} are given by the Eqs. (23) and (24). Fig. 6 shows the equivalent circuit used. Both parameters are combined in Eq. (28), to calculate $Z_{eq}[\Omega]$, which is the total impedance of the motor.

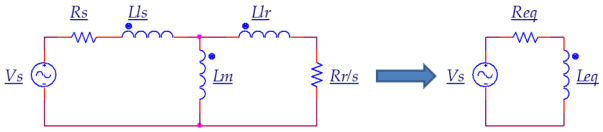

FIGURE 6. Equivalent circuit under standstill conditions.

$$Z_{eq} = R_{eq} + j\cdot X_{eq} = \underbrace{\left[R_s + \frac{\omega_e^2\cdot L_m^2\cdot R_r}{R_r^2+\omega_e^2\cdot L_r^2}\right]}_{R_{eq}} + j\cdot\underbrace{\left[L_S - L_m + \frac{L_m\cdot\left[R_r^2+\omega_e^2\cdot L_r\cdot(L_r-L_m)\right]}{R_r^2+\omega_e^2\cdot L_r^2}\right]}_{X_{eq}} \quad (28)$$

Equation (25) defines the dimensionless parameter β, which establishes the relationship between the magnetizing inductance and the secondary inductance. Equation (26) describes the mechanical thrust force $F_y[N]$ developed by the TFLIM. To obtain this value, a simulation is carried out with FEM-3D under nominal conditions. This condition considers a frequency equal to 50 Hz and a linear velocity of the secondary part equal to 0 m/s or a slip equal to one. The average value of the thrust force with the restrictions is around 80 N [25]. Equation (26) has been defined by two terms, which indicate the two thrust forces that generate the TFLIM. The first one $F_{y1}[N]$ is the thrust force produced by the slip current and it is a positive thrust. However, the second one $F_{y2}[N]$ is the thrust force produced by the demagnetizing loss and it is always negative. F_y is calculated as a sum of both forces. Analysing F_{y1} it can be observed that it depends on four variables: (1) the secondary electrical current per phase $I_2[A]$, (2) the secondary resistance $R_r[\Omega]$, (3) the pole pitch $\tau_p[mm]$ and (4) $\omega_2[rad/s]$ which is the slip angular frequency. Furthermore, for a slip equal to one, $F_{y2}[N]$ depends on the magnetizing current $I_m[A]$ and on the sum between the leakage secondary inductance L_{lr}[H] and the magnetizing inductance, $L_m[H]$.L = 503.5 mm. is the length of the TFLIM.

Equation (27) describes the second Kirchhoff's law applied to our equivalent circuit where the electric current from de voltage source $I_s[A]$ is divided into the magnetizing current and secondary current. I_s is obtained under nominal conditions as an average value of the electric current of each phase (Eq. (29)).

$$I_s = \left(i_{phase_a} + i_{phase_b} + i_{phase_c}\right)/3 \quad (29)$$

where i_{phase_a}[A], i_{phase_b}[A] and i_{phase_c}[A] are the absorbed electric current in each phase. To define all parameters described in Table 1, it is necessary to define two relationships between the values of the inductances according to the

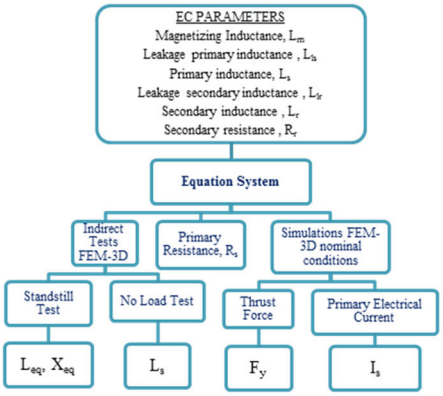

FIGURE 7. Diagram process to solve the equation system.

Eqs. (30) and (31):

$$L_s = L_m + L_{ls} \tag{30}$$

$$L_r = L_m + L_{lr} \tag{31}$$

Fig. 7 shows the diagram process used to correctly solve the system of equations. It is important to remark that the proposed system of equations is provided with solutions of different forms. So, we can summarize the process in the following three steps according to the three blocks illustrated in the Fig. 7:

1. Data from indirect tests: The standstill test is necessary to estimate the total resistance and reactance from our TFLIM and the no load test give us an accurate way to estimate the primary inductance.
2. Data from simulations under nominal conditions: This simulation is needed to obtain the value of the thrust force developed by the TFLIM and the measurement of the electric current absorbed by each phase, when TFLIM operates under nominal conditions.
3. Data to compute the primary resistance: We have considered the particularities of the primary winding, where the special coils locations influence considerably in the total DC resistance value. In this case, it is not necessary to run a simulation to calculate the DC resistance value because it can be obtained numerically. In further sections, this value will be modified to add the skin effect inside conductors of a multilayer winding.

Table 6 summarizes all variables involved in the system of equations. The variables are classified in three categories: variables obtained by FEM-3D, corresponding with the type of indirect tests used, variables defined by the designer, which are unknown, and variables that must be estimated. The right hand side of Table 6 shows the selected frequencies used in the different tests. There are six experiences that use indirect tests.

V. RESULTS

This section describes the simulation results using FEM-3D. The section is divided into two subsections. Subsection V-A shows the results once both electrical tests have been simulated. This subsection is also divided into two. First subsection V-A1) describes the standstill test results and the general equations to numerically predict value of the total resistance and impedance numerically, when the motor operates under other frequency ranges. Subsection V-A2) analyses the no load test and proposes a general equation to estimate the primary inductance per phase linked to our TFLIM, when the motor operates in other frequency ranges. In subsection V-B the EC parameters are obtained using the system of equations proposed above. We have divided this subsection in two. Subsection V-B1) focuses on the analysis of the results from primary part parameters where we have studied some specific phenomena and subsection V-B2), where we study the secondary parameters obtained and compare them with the results obtained by applying the 2-D Field Theory to our TFLIM.

TABLE 6. Variables involved for solving EC applied to TFLIM.

Classification of the variables in the equations system				Frequencies simulation [Hz]					
Variables obtained by FEM-3D		Defined variables	Unknown Variables	Test 1	Test 2	Test 3	Test 4	Test 5	Test 6
Standstill test	$R_{eq}[\Omega]$	$\omega_2[rad/_s]$ $\tau_p[mm]$ $L[mm]$ β	$L_m[H]$	55	60	70	80	90	100
	$L_{eq}[H]$		$L_r[H]$						
No load test	$L_S[H]$		$R_r[\Omega]$	18	16	14	12	10	8
Nominal conditions	$F_y[N]$		$I_2[A]$	50					
	$I_s[A]$		$I_m[A]$						

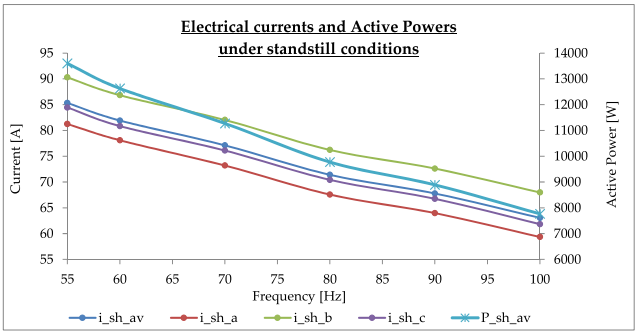

FIGURE 8. Electric currents and active power absorbed under standstill conditions.

A. RESULTS FROM INDIRECT TESTS IN FEM-3D

1) RESULTS FROM STANDSTILL CONDITIONS

The experiments have been simulated using indirect tests under standstill conditions, so the secondary part is blocked. Fig. 8 shows the behaviour of electric currents for each phase, i_{sh_b} [A], i_{sh_b} [A] and i_{sh_b} [A], the average values of active power, $P_{_sh_av}[W]$ and the average electric current, $i_{_sh_av}$ [A].

Electric currents follow a uniform distribution due to the following phenomena:

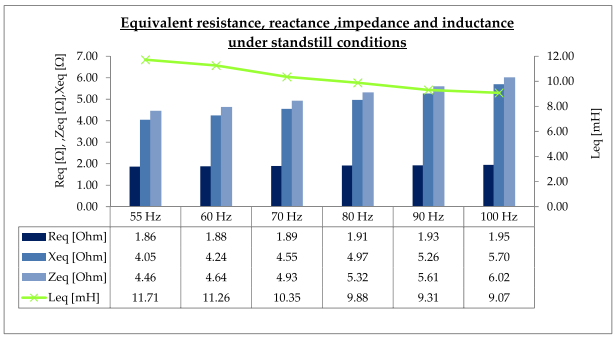

FIGURE 9. Total impedance, reactance, resistance, and inductance under standstill conditions.

1. The TFLIM is an unbalanced three-phase system of electric currents due to the dynamic end-effect. The electric current from phase B, $i_{_sh_b}$, absorbs the most current and the electric current from phase A, $i_{_sh_a}$, consumes less current than the other two phases. This behaviour is same in all tests. The difference between the electric current from phase A and phase B cannot be neglected. This effect is very important to identify parasite thrust forces generated during the tests.
2. The difference between the average value of electric current and the electric currents per phase determine the maximum and minimum deviation from the average value, $i_{_sh_av}$ (see Eq. (32)). Table 7 collects this deviation using parameters $\Delta i_{max}[\%]$ and $\Delta i_{min}[\%]$ according to Eq. (33):

$$i_{sh_av} = \frac{i_{sh_a} + i_{sh_b} + i_{sh_c}}{3} \tag{32}$$

$$\Delta i_{max}\,(\%) = \left|\frac{i_{sh_b} - i_{sh_{av}}}{i_{sh_{av}}}\right| \cdot 100 \;\; \Delta i_{min}(\%) = \left|\frac{i_{sh_a} - i_{sh_av}}{i_{sh_av}}\right| \cdot 100 \tag{33}$$

   Δi_{max} determines the variation of i_{sh_b} with respect to i_{sh_av}, which is around 10 % in all tests except test 1 where it is only 5% and test 6 where it reaches 12 %. The deviation from Δi_{min} is smaller and its value is between 4.78% for test 1 and 5.85% for test 6.
3. In Fig. 8 we observe that when the frequencies increase the electric currents per phase decrease. So, an increment of frequencies implies an increment of the impedance of the primary part in the equivalent circuit (see Eq. (34)).

$$I_{sh_av} = {}^{V_{LINE}}\!/_{R_{eq} + 2 \cdot \pi \cdot f \cdot L_{eq}} \tag{34}$$

Fig. 9 shows the parameters obtained from the simulations under standstill conditions. The first parameter L_{eq} [mH] is between 11.71 mH and 9.07 mH and slowly decreases as the frequency increases. The second parameter, R_{eq} [Ω], changes from 1.86 Ω to 1.95 Ω as the frequency increases. With these parameters, we can calculate the equivalent reactance X_{eq} [Ω] and the equivalent impedance Z_{eq} [Ω]. The impedance varies between 4.46 Ω and 6.02 Ω and represents the total resistance of the equivalent circuit without movement in the secondary part. To validate the simulation results, we have checked the agreement between the positive increase in Z_{eq} and the decrease in I_{sh_av} absorbed by the TFLIM.

TABLE 7. Deviations of electric currents under standstill conditions.

Electric Current	Test 1	Test 2	Test 3	Test 4	Test 5	Test 6
$i_{_sh_a}$ [A]	81.249	78.097	73.196	67.572	63.976	59.356
$i_{_sh_b}$ [A]	90.273	86.830	82.030	76.219	72.614	67.982
$i_{_sh_c}$ [A]	84.454	80.842	76.110	70.427	66.747	61.834
$i_{_sh_av}$ [A]	85.325	81.923	77.112	71.406	67.779	63.057
Δi_{max} (%)	5.798	10.057	10.770	11.344	11.897	12.688
Δi_{min} (%)	4.778	4.670	5.079	5.369	5.611	5.869

L_{eq}, X_{eq} and Z_{eq} for higher frequencies can be approximated by a linear curve, using a least square linear regression method. With a selected set of elements (x_1, y_1), $(x_2, y_2), \ldots, (x_i, y_i)$, the regression method finds a linear function defined by two parameters a and b (see Eq. (35)). Both, a and b are calculated by Eqs. (36) and (37), where $\bar{x}$ and $\bar{y}$ corresponds to the average values of the selected elements (see Eqs. (38) and (39)). For more details see references [29], [30], [31].

$$y = a \cdot x + b \tag{35}$$

$$a = \sum_{i=1}^{n} (x_i - \bar{x}) \cdot (y_i - \bar{y}) \big/ (x_i - \bar{x})^2 \tag{36}$$

$$b = \bar{y} - a \cdot \bar{x} \tag{37}$$

$$\bar{x} = \sum_{i=1}^{n} x_i / n \tag{38}$$

$$\bar{y} = \sum_{i=1}^{n} y_i / n \tag{39}$$

In this paper, x is the frequency linked to the voltage source and y is the value of L_{eq}, X_{eq} and Z_{eq}. Equations (40), (41) and (42) define the variables L_{eq_0} [mH], R_{eq_0} [Ω] and X_{eq_0}[Ω]. They are the values of these parameters at the starting point. m_L, m_R and m_X are the slopes of these linear curves.

$$L_{eq} = L_{eq_0} + m_L \cdot f \tag{40}$$

$$R_{eq} = R_{eq_0} + m_R \cdot f \tag{41}$$

$$X_{eq} = X_{eq_0} + m_X \cdot f \tag{42}$$

Table 8 shows the final equations that predict these variables for higher frequencies. This prediction has been made without simulation.

Fig. 10 represents the evolution of the main forces of a TFLIM. The secondary part has three degrees of freedom, so its displacement uses three axes. This item is very important to identify this effect in the laboratory where thrust, normal and vertical forces can be measured using load cells. $F_{x_{sh}}[N]$, $F_{y_sh}[N]$ and $F_{z_sh}[N]$ are the lateral, thrust and

TABLE 8. Equations obtained from least square linear regression.

L_{eq}		R_{eq}		X_{eq}	
L_{eq_0} $[mH]$	m_L	$R_{eq_0}[\Omega]$	m_R	X_{eq_0} $[\Omega]$	m_X
14.7759	−0.05948	1.766742	0.0018042	2.568416	0.0342192
$L_{eq} = -0.05948 \cdot f + 14.7759$		$R_{eq} = 0.0018042 \cdot f + 1.766742$		$Z_{eq} = 0.0342192 \cdot f + 2.568416$	

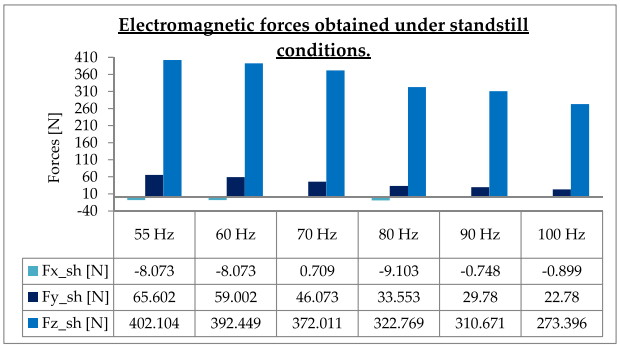

	55 Hz	60 Hz	70 Hz	80 Hz	90 Hz	100 Hz
Fx_sh [N]	-8.073	-8.073	0.709	-9.103	-0.748	-0.899
Fy_sh [N]	65.602	59.002	46.073	33.553	29.78	22.78
Fz_sh [N]	402.104	392.449	372.011	322.769	310.671	273.396

FIGURE 10. Electromagnetic forces obtained under standstill conditions.

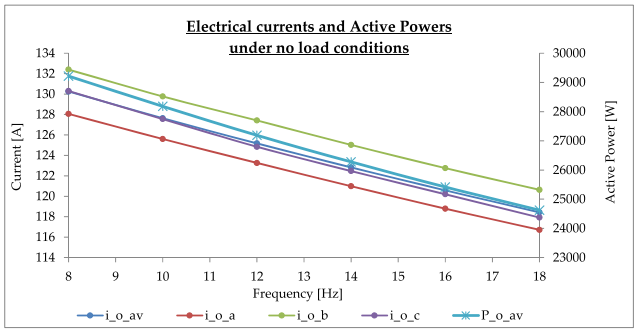

FIGURE 11. Electric currents and active power absorbed under no load conditions.

normal forces respectively. In FEM-3D these forces are simulated as an average value obtained after the transitory state.

The transversal forces are not relevant compared to others. Transversal or lateral forces are consequence of the dynamic and static end effect. The lateral force varies from -9.1 N to -0.8 N. This behaviour cannot be predicted but needs to be considered to control the system. The evolution of thrust and normal force is relevant, since when the frequency increases the forces decrease. Thrust force decreases around 42.822N from the initial frequency to the final frequency. Vertical force decreases 128.78 N under the same conditions.

2) RESULTS FROM NO LOAD CONDITIONS

The absorbed electric currents have shown in Fig. 11. Although the simulation operates at low frequencies, the system is also unbalanced.

Table 9 shows the absorbed electric current by each phase, $i_{o_a}[A]$, $i_{o_b}[A]$ and $i_{o_c}[A]$. Phase A presents the lower absorbed electric current. Phase B current is the most

TABLE 9. Deviations of electric currents under no load conditions.

Electric Current	Test 1	Test 2	Test 3	Test 4	Test 5	Test 6
i_{o_a} [A]	116.716	118.788	120.987	123.261	125.601	128.059
i_{o_b} [A]	120.632	122.754	125.028	127.417	129.770	132.395
i_{o_c} [A]	117.921	120.194	122.468	124.845	127.552	130.297
i_{o_av} [A]	118.423	120.579	122.828	125.174	127.641	130.250
$\Delta i_{máx}$ (%)	1.865	1.804	1.791	1.791	1.668	1.646
Δi_{min} (%)	1.441	1.485	1.498	1.528	1.598	1.682

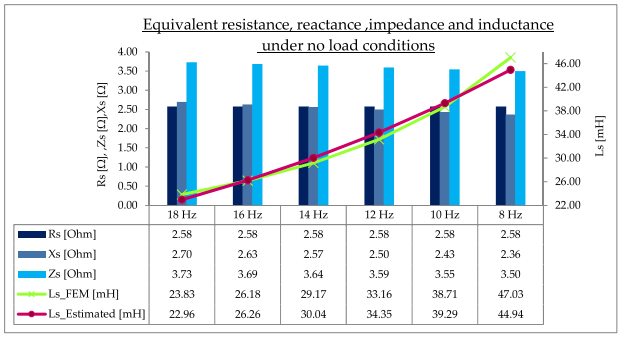

	18 Hz	16 Hz	14 Hz	12 Hz	10 Hz	8 Hz
Rs [Ohm]	2.58	2.58	2.58	2.58	2.58	2.58
Xs [Ohm]	2.70	2.63	2.57	2.50	2.43	2.36
Zs [Ohm]	3.73	3.69	3.64	3.59	3.55	3.50
Ls_FEM [mH]	23.83	26.18	29.17	33.16	38.71	47.03
Ls_Estimated [mH]	22.96	26.26	30.04	34.35	39.29	44.94

FIGURE 12. Electric parameters under no load conditions.

restrictive. The average value of the absorbed electric current, $i_{o_av}[A]$ (see Eq. (43)), when the frequencies go from 8 Hz to 18 Hz, decreases from 130.250 A to 118.423 A. In addition, the average value of active power, $P_{o_av}[W]$ also decreases. Thus, for frequencies between 18 Hz and 8 Hz the active power varies from 29.2 KW to 24.7 KW.

Table 9 also includes the maximum and minimum deviation of the electric current respect to its average value, $\Delta i_{\max_o}$ (%) and $\Delta i_{\min_o}$ (%). Both parameters will be estimated by Eq. (44) and give similar results, not exceed 2% of the average value. Therefore, it can be concluded that under no load conditions the unbalance system of electric current is less relevant than when the tests are simulated under standstill conditions.

$$i_{o_av} = \frac{i_{o_a} + i_{o_b} + i_{o_c}}{3} \tag{43}$$

$$\Delta i_{max_o}\,(\%) = \left|\frac{i_{o_b} - i_{o_av}}{i_{o_av}}\right| \cdot 100 \;\Delta i_{min_o}(\%) = \left|\frac{i_{o_a} - i_{o_{av}}}{i_{o_{av}}}\right| \cdot 100 \tag{44}$$

Now, we are going to calculate the electric parameters from the equivalent electric circuit. Fig. 12 shows the primary inductance (from Eq. (21)) and the primary inductance $L_s[H]$ as well as the primary impedance $Z_s[\Omega]$, primary reactance $X_s[\Omega]$ and primary resistance $R_s[\Omega]$ from the equivalent circuit. $L_{s_FEM}[mH]$ is the primary inductance obtained by FEM-3D and $L_{s_{Estimated}}[mH]$ the same value predicted with the regression method, using Eqs. (45), (46) and (47) (see

TABLE 10. Values of coefficients, a and b, obtained by linear regression.

Coefficients	No Load Tests					
	8 Hz	10 Hz	12 Hz	14 Hz	16 Hz	18 Hz
a	-0.067	-0.067	-0.067	-0.067	-0.067	-0.067
b	76.905	76.905	76.905	76.905	76.905	76.905

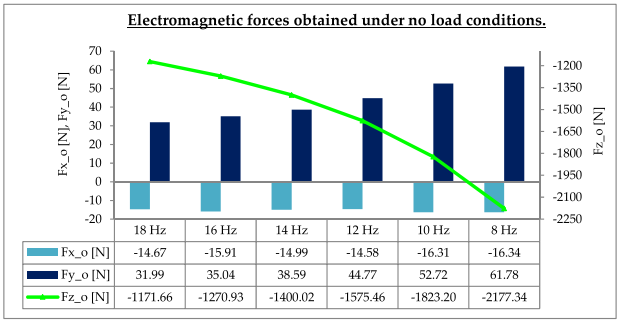

FIGURE 13. Electromagnetic forces obtained under no load conditions.

references [29], [30], [31] for more details).

$$L_s = b \cdot e^{a \cdot f} \tag{45}$$

$$a = n \cdot \sum_{i=1}^{n} ln\ (y_i) \cdot x_i - \left(\sum_{i=1}^{n} x_i\right) \cdot \left(\sum_{i=1}^{n} ln\ (y_i)\right) \Big/ n \cdot \left(\sum_{i=1}^{n} x_i^2\right) - \left(\sum_{i=1}^{n} x_i\right)^2 \tag{46}$$

$$b = exp\left({}^{1}\!/_{n} \cdot \sum_{i=1}^{n} ln\,(y_i) - \frac{a}{n} \cdot \left(\sum_{i=1}^{n} x_i\right)\right) \tag{47}$$

Table 10 shows the parameters a and b by different frequencies using the linear regression method.

The values of the variables L_s, L_{s_FEM} and $L_{s_{Estimated}}$ are similar. When the frequency decreases, the inductance increases from 23 mH to 47 mH and X_s is usually constant. The reason is the double effect developed by the variations of the frequencies and inductances that counteract each other as shown in Eq. (19).

Fig. 13 shows the generated forces. Now the electromagnetic forces are different with respect to the forces obtained under standstill condition. Although the tests operate under no load conditions, the thrust force is not equal to zero, due to the dynamic end-effect. The value of the thrust force increases considerably for these frequencies. Its variation is around 29.8 N, a double increase with respect to the initial thrust force. The transversal force cannot be neglected either because varies between -14.6 N and -61.8 N. Now, vertical forces are attractive whereas under standstill conditions, vertical forces were repulsive. Vertical forces have two orders of magnitude larger than the other forces, so they have been represented separately by a line chart. The simulation shows the rise of these forces when the frequency reaches a maximum value around -2177 N for the lowest frequency.

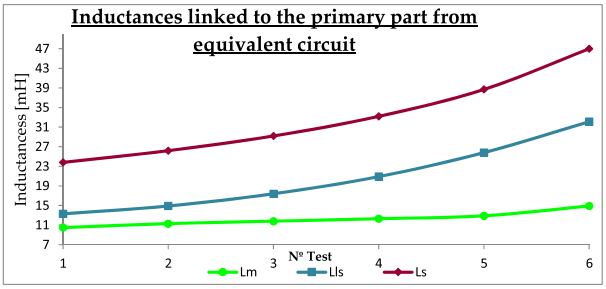

FIGURE 14. Inductances of the primary part of the TFLIM.

B. EC PARAMETERS RESULTS USING EQUATIONS SYSTEM

This section presents the parameters needed to implement the equivalent circuit using the system of equations from (23) to (27). The parameters can be divided into two groups, parameters of the primary part, L_m, L_{ls}, L_s and R_s and the secondary part L_r, L_{lr} and R_r.

1) ANALYSIS OF THE PRIMARY PART EC PARAMETER

There are two very important variables in electric machines, main flux $\boldsymbol{\phi_m}$ and leakage flux $\boldsymbol{\phi_\sigma}$. The main flux must cross the electromagnetic air gap of a TFLIM, so primary and secondary parts are connected electromagnetically. ϕ_m creates an air gap flux linkage $\boldsymbol{\psi_m}$ that joins the two parts. Furthermore, the leakage fluxes of the primary and secondary part do not cross the air gap and generate a total flux link of the winding through a leakage flux link ψ_σ. Then, total flux leakage is divided into the flux leakage $\boldsymbol{\psi_{s\sigma}}$ of the primary part and the flux leakage of the secondary part $\boldsymbol{\psi_{r\sigma}}$. Therefore, it can be concluded that air gap flux linkage corresponds to the magnetizing inductance $\boldsymbol{L_m}$, and the leakage flux linkage to a leakage inductance $\boldsymbol{L_\sigma}$ [25]. The first is a very important variable in TFLIM.

Fig. 14 represents the behaviour of L_m. L_m varies between 10.5 mH and 14.5 mH. Leakage inductance L_{ls} between 13.3 mH and 32.1 mH, greater than L_m. L_{ls}/L_m, determines the relevance of the leakage inductance, where the value of non-useful flux can reach up to twice the magnetizing flux as checked in test 5 and test 6. The leakage magnetic flux $\Psi_{s\sigma}[Wb]$ depends from the contribution of various leakage fluxes. In this paper, these fluxes are not calculated but it is necessary to identify them to better understand the physical phenomenon involved in the process.

Table 11 shows the parameters of the primary part of the equivalent circuit. The magnetizing current per phase, I_m decreases from 13.3 A. to 6.2 A. However, the primary current (I_s) maintains the same value set at 90 A. in all simulations under nominal conditions. Table 11 also shows the leakage flux. This flux is predominant in our model because the transversal flux is greater than the longitudinal flux. All simulated tests show this effect when leakage flux ($\Psi_{s\sigma}$) is greater than the magnetizing flux (Ψ_m). The difference between both fluxes increases considerably, so that in Test 6

TABLE 11. Primary part parameters from equivalent circuit.

Primary part parameters obtained by indirect tests						
N° Test	*Test 1*	*Test 2*	*Test 3*	*Test 4*	*Test 5*	*Test 6*
$L_m[mH]$	10.500	11.300	11.800	12.300	12.900	14.900
$L_{ls}[mH]$	13.300	14.900	17.400	20.900	25.800	32.100
$L_s[mH]$	23.800	26.200	29.200	33.200	38.700	47.000
$L_m[mH]/Lls\ [mH]$	1.267	1.319	1.475	1.699	2.000	2.154
$I_m\ [A]$	13.344	11.282	12.218	13.154	14.091	6.201
$I_s[A]$	90.000	90.000	90.000	90.000	90.000	90.000
$\psi_m[Wb]$	140.113	127.485	144.174	161.798	181.767	92.390
$\psi_{s\sigma}[Wb]$	1197.000	1341.000	1566.000	1881.000	2322.000	2889.000
$\psi_s[Wb]$	1337.113	1468.485	1710.174	2042.798	2503.767	2981.390

the magnetizing flux only reaches a value close to 92.3 Wb. while the leakage flux increases approximately 2890 Wb.

The leakage inductance L_{ls} is calculated by the Eq. (48):

$$L_{ls} = L_{sq} + L_{\delta} + L_u + L_d + L_w \tag{48}$$

where:

- $L_{sq}[mH]$: **Skew leakage inductance.** In a LIM, the slots are often assembled skewed from each other to reduce the influence of the harmonic created by them. In our research, this does not apply because this inductance is neglected.
- $L_{\delta}[mH]$: **Air gap leakage inductance.** Due to slotting along the primary part, the harmonics linked to the magnetic field density along the air gap induce non-desired voltages. We only consider the fundamental harmonics which contribute to the magnetizing inductance.
- $L_{\delta}\ [mH]$: **Slot leakage inductance.** This inductance is very important because it has been created by a real leakage flux. This effect is relevant in double-layer windings because there are slots with coils in two different phases. The traverse magnetic circuit presents an open slot that intensifies this effect because the slots that generate the longitudinal magnetic circuit are not closed by a ferromagnetic yoke. Both reasons imply high notch leakage inductances.
- $L_d\ [mH]$: **Tooth tip leakage inductance.** This inductance is determined by the leakage flux which flows in the air gap outside the slot opening. We consider that slots are open completely, so this leakage flux is not relevant.
- $L_w\ [mH]$: **End winding leakage inductance.** This leakage flux results from currents of the end windings. In TFLIM this effect is smaller than in LFLIM, due to the flux generated by the end winding, will cross the air gap through the lateral teeth.

To complete the analysis of the primary part, we need to analyse three specific phenomena, which are relevant in the equivalent circuit: skin effect, fringing effect and the influence of the primary slot opening on the equivalent magnetic air gap.

a: SKIN EFFECT IN A TFLIM

This phenomenon appears because there is an alternating current in a conductor which produces an alternating flux within the conductor of the armature. This effect increments the DC resistance linked to the conductor material. To estimate it, it is necessary to define the following parameters used in equations (49) to (53):

1. **Computation of α**: It is the propagation coefficient defined by Eq. (49), where $\mu_0 = 4 \cdot \pi \cdot 10^{-7} {}^{H}/_{m}$ is the magnetic permeability of free space μ_0, $\sigma_{copper} = 4.21 \cdot 10^7 S \cdot m^{-1}$ is the copper conductivity and $\omega_e \left[{}^{rad}/_{s}\right]$ is the source electrical angular frequency. f[Hz] is set at 50 Hz and finally $\rho_{penetration}\ [m]$ is the penetration depth [3].

$$\alpha = \sqrt{\mu_0 \cdot \sigma_{copper} \cdot \omega_e / 2} = 1/\rho_{penetration} \tag{49}$$

2. **Estimation of ξ:** This coefficient can be defined using a dimensionless number defined by Eq. (50), where $h_{slot}[m]$ is the height of the slot.

$$\xi = \alpha \cdot h_{slot} \tag{50}$$

3. **Computation of K_{Rac}**: A dimensionless parameter necessary to quantify the skin effect. R_{s_dc} has been explained before and it is the DC value of the resistance per phase, as in (51), shown at the bottom of the next page.
4. **Computation of K_{Rmac}**: Using Eq. (52), with the dimensionless parameters K_{Rmac}, we can correct the skin effect. The AC resistance value is adapted to windings with a number of layers other than one. Variable m considers the number of layers of a double layer windings configuration, where m is equal to 2.

$$\begin{aligned} K_{Rmac} &= K_{Rac} + \left({}^{(m^2-1)}/_{3}\right) \cdot \Psi'(\xi) \\ &= K_{Rac} + \left({}^{(m^2-1)}/_{3}\right) \\ &\quad \cdot (sinh(\xi) + sin(\xi)/((cosh(\xi) + cos(\xi)) \cdot \xi)) \end{aligned} \tag{52}$$

5. **Estimation of equivalent resistance for alternating current**: Eq. (53) determines the estimation of the primary resistance of a primary winding operating under alternating current and adapted to the number of layers.

$$R_{s_ac} = R_{s_dc} \cdot K_{Rmac} \tag{53}$$

Table 12 shows relevant information about skin effect phenomenon. Its design involves open slots and therefore the primary resistance is incremented considerably with respect to the DC value. In our work, there is a double layer winding, therefore the coefficient K_{Rmac} reaches a value around 4.2 and the resistance per phase increases up to 11 Ω.

For example, in the RIM case for a rectangular squirrel cage bar, the resistance factor can reach even values close to 5 Ω.

TABLE 12. Skin effect parameters in a double layer TFLIM.

Skin Effect Parameters					
$\rho_{penetration}\,[m]$	ξ	K_{Rac}	K_{Rmac}	R_{s_dc} [Ω]	R_{s_ac} [Ω]
0.01095	4.0155	4.0176	4.2654	2.58	11.0046

b: EFFECTIVE AIR GAP AND CARTER'S COEFFICIENT ESTIMATION

Once L_m is known the effective air gap g_{ef} and Carter's coefficient K_c are defined by Eqs. (54) to (57). For this, we must know the difference between three air gaps characteristics, $g_{mec}[mm]$, $g_{elm}[mm]$ and $g_{ef}[mm]$ [31]. g_{mec} is the physical separation between primary and secondary part, g_{elm} the distance between the mechanical air gap and the thickness of the aluminium sheet and g_{ef} considers that the air gap flux density varies with the primary slot openings, so it produces an equivalent effect equivalent to a larger constant air gap. The flux density always decreases at the slot opening according to Carter's principle, although the physical air gap appears to be larger than the physical measurement of this dimension [25], [32]. In the classic longitudinal linear induction motor, the value of Carter's coefficient $\boldsymbol{K_c}$ ranges from 1.1 to 1.7 and is defined by Eq. (54).

$$K_c = \left[6 \cdot \mu_0 \cdot (W_1 \cdot K_{w1})^2 \cdot \tau_p \cdot L_{TFLIM}\right] \Big/ \left[g_{mec} \cdot (1 + k_{ss}) \cdot \pi^2 \cdot L_m\right] \tag{54}$$

where $\mu_0 = 4 \cdot \pi \cdot 10^{-7} H/_m$ is the magnetic permeability on free space; $W_1 = 44$ is the number of turns per phase, $K_{w1} = 0.6773$ is the winding factor, $\tau_p = 200\ mm$ is the pole pitch, $L_{TFLIM} = 503.5\ mm$ is the length of the primary part steel sheet along a transverse section, $K_{ss} = 1$ is the saturation factor and $g_{mec} = 5\ mm$ is the mechanical air gap.

The electromagnetic air gap, g_m is given by Eq. (55), where K is equal to 1 in a single sided TFLIM and equal to 2 in a double sided TFLIM. In our work, K is equal to 1 and $h_{Al} = 10\ mm$, that is the thickness of the aluminium layer.

$$g_{elm} = k \cdot g_{mec} + h_{Al} = 15\ mm. \tag{55}$$

The value of the effective air gag is calculated by Eq. (57), which includes the fringing effect. This phenomenon is shown in Fig. 15. It shows how the magnetic flux lines do not follow a straight line, so the path is longer than the electromagnetic air gap. To evaluate this effect, it is used a dimensionless parameter called fringing coefficient, K_{Fr} defined by Eq. (56).

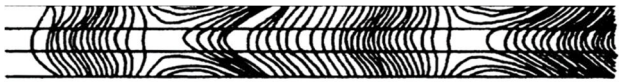

FIGURE 15. Fringing effect in a double-sided LIM [32].

TABLE 13. Carter's coefficient and characteristic air gaps.

N° test	Test 1	Test 2	Test 3	Test 4	Test 5	Test 6
K_c	1.301	1.209	1.158	1.110	1.059	0.917
$K_{c_average}$	1.126					
g_{ef} [mm]	19.5205	18.1385	17.3699	16.6638	15.8888	13.756
$g_{ef_average}$ [mm]	16.890					
g_{mec} [mm]	5					
g_{elm} [mm]	15					

$$K_{Fr} \approx sinh\left(\frac{g_{mec}}{2 \cdot \tau_p}\right) \Big/ \left(\frac{g_{mec}}{2 \cdot \tau_p}\right) = 1 \tag{56}$$

$$g_{ef} = g_{mec} \cdot K_c \cdot K_{Fr} \tag{57}$$

Table 13 collects these relationships where all the air gap categories are estimated for each test.

In Table 13, the average values of K_c and g_{ef} are also calculated using $K_{c_average}$ and $g_{ef_average}$ respectively. The value of $K_{c_average}$ is within the recommended limits for longitudinal flux, so the effect of this shape of ferromagnetic sheet in the primary part with this type of slot does not drastically influence in a longer effective air gap, whose average value reaches 16.89 mm. The $g_{ef_average}$ value increases around 12 % with respect to the electromagnetic air gap. Consequently, this increment in the effective air gap implies a higher magnetizing current for the generation of the magnetomotive force necessary to establish the value of the magnetic field along the air gap.

c: MAGNETIZING INDUCTANCE ESTIMATION FROM MAGNETIC FIELD DENSITY

To validate the main EC parameters, the L_m obtained from indirect test must be checked. Firstly, we use an analytical method and secondly we present the results obtained and its

$$\begin{aligned} R_{S_ac} &= R_{S_dc} \cdot K_{Rac} \\ &= \underbrace{\frac{n_{phase} \cdot \left(\rho_{Cu} \cdot \bar{L}_{coil} \cdot N_{phase}\right)}{S_c}}_{R_{Sdc}} \\ &\quad \cdot \underbrace{\xi(\cdot sinh(2 \cdot \xi) + sin(2 \cdot \xi)/cosh(2 \cdot \xi) - \cos(2 \cdot \xi))}_{K_{Rac} \geq 1} \end{aligned} \tag{51}$$

comparison with the simulation data. A classical analysis of TFLIM uses an equivalent circuit whose magnetizing branch separates longitudinal and transversal inductances. In this paper, both inductances are considered using a method with the measurements of the magnetic field along the air gap.

The amplitude of the magnetomotive force along the air gap can be approximated to the module of the first harmonic. This approximation is denoted by $A_{max}[A \cdot m]$ using Eq. (58), where $N_p[n^{\underline{o}}\ turns]$ is the value of turns per phase and pole, $I_{\emptyset}[A]$ is the magnetizing current without secondary part coupled and K_{w1} is the winding factor.

$$A_{max} = {4 \cdot \sqrt{2}}/{\pi} \cdot \left(N_p \cdot I_{\emptyset}\right) \cdot m \cdot K_{w1} \tag{58}$$

The magnetic field density along the air gap $B_{\delta_max}[T]$ is defined by Eq. (59). It is proportional to the quotient between A_{max} and the air gap $\delta\,[mm]$, where $\mu_0 = 4 \cdot \pi \cdot 10^{-7} {H}/{m}$.

$$\begin{aligned} B_{\delta_max} &= \mu_O \cdot {A_{max}}/{\delta} \\ &= \mu_O \cdot \left({4 \cdot \sqrt{2}}/{\pi} \cdot \left(N_p \cdot I_{\emptyset}\right) \cdot m \cdot K_{w1}\right) \Big/ {2 \cdot \delta} \end{aligned} \tag{59}$$

Magnetic flux is calculated by Eq. (60), where $L_{TFLIM}[mm]$ is the length of the TFLIM, p is the number of pair of poles and $w\,[mm]$ is the width of the TFLIM. Induced voltage $E_{ind}[V]$ is computed by Eq. (61). Using the previous relationships, the magnetizing reactance is determined by Eq. (62) and the magnetizing inductance per phase by Eq. (63).

$$\emptyset_{max} = B_{\delta_max} \cdot {L_{TFLIM}}/{2 \cdot p} \cdot w \tag{60}$$

$$\begin{aligned} E_{ind} &= \sqrt{2} \cdot \pi \cdot N_P \cdot f \cdot \xi_t \cdot \emptyset_{max} \\ &= \sqrt{2} \cdot B_{\delta_max} \cdot \pi \cdot N_P \cdot f \cdot K_{w1} \cdot {L_{TFLIM}}/{2 \cdot p} \cdot w \end{aligned} \tag{61}$$

$$\begin{aligned} \chi_m &= {E_{ind}}/{I_{\emptyset}} \\ &= 4 \cdot \pi \cdot \frac{m \cdot f \cdot \left(N_p \cdot K_{w1}\right)^2 \cdot L_{TFLIM} \cdot w}{\delta} \end{aligned} \tag{62}$$

$$\begin{aligned} L_m &= \left({E_{ind}}/{I_{\emptyset}}\right) \cdot \frac{1}{\omega_e} \\ &= \left({E_{ind}}/{I_{\emptyset}}\right) \cdot \frac{1}{2 \cdot \pi \cdot f} \end{aligned} \tag{63}$$

These four equations are used to calculate the magnetizing inductance per phase applied to our motor. Our TFLIM has a main flux which operates across a transversal plane. However, the particular location of the coils in the primary winding along four layers implies that not only the transversal flux is going to cross the air gap, so that longitudinal magnetic flux could appear. For this reason, to estimate L_m, it is necessary to consider all magnetic fluxes, transversal and longitudinal. For this, it must be considered the geometric differences between the transversal and longitudinal magnetic circuits. And it is assumed that in both cases the effective air gap is the mechanical air gap. At last, net magnetizing reactance per phase can be computed by Eq. (64).

$$\chi_m = \chi_{m_long} + 2 \cdot \chi_{m_trv} \tag{64}$$

Using FEM-3D, TFLIM has been simulated considering two conditions:

1. Eddy current induced in the secondary aluminium layer is not considered, so the TFLIM is simulated with secondary part open.

2. The moving part is blocked, so TFLIM operates under standstill conditions. Then, the electric conductivity of the aluminium layer is zero and consequently no eddy currents can be induced. With this restriction, the magnetic field density along the air gap is measured. With FEM-3D it can be simulated using a longitudinal path along the length of the TFLIM located on a medium plane that divides the mechanical air gap. Then, it is possible to know the density of the magnetic field along transversal direction $B^z_{\delta_max}[T]$ and the magnetic field along the longitudinal direction $B^y_{\delta_max}[T]$. Additionally, with these variables it can be obtained the magnetizing current without secondary part coupled and the induced voltage for each magnetic field density.

Next, we are going to adapt the process described above by analysing the transversal magnetic flux and longitudinal magnetic flux measured across the air gap.

Case a) Analysis of Transversal Flux: Equation (65) defines the transverse magnetizing reactance $X_{trv}[\Omega]$. Eq. (62) is adapted to this type of magnetic flux. Then, Eq. (65) defines this reactance as a quotient between the induced voltage due to the transverse magnetic flux, $E_{\text{ind_trv}}[V]$, and the magnetizing current, $I_{\emptyset_\text{trv}}[A]$, necessary to create the transverse magnetic flux.

$$X_{trv} = {E_{\text{ind_trv}}}/{I_{\emptyset_\text{trv}}} \begin{cases} E_{\text{ind_trv}} = \sqrt{2} \cdot \pi \cdot N_P \cdot f \cdot K_{w1} \cdot B^z_{\delta_max} \\ \qquad \cdot \left({L_{trv}}/{2 \cdot p}\right) \cdot w_{trv} \\ I_{\emptyset_\text{trv}} = \cdot B^z_{\delta_max} \cdot \pi \cdot \delta_{mec} / 6 \cdot \sqrt{2} \\ \qquad \cdot \mu_O \cdot K_{w1} \cdot N_P \end{cases} \tag{65}$$

where $L_{trv} = 400\ mm.$ is the length of the TFLIM for two pole pitches. If we take into account the symmetry linked to the central tooth, w_{trv} can be estimated by Eq. (66) where $w_{central_tooth} = 48\ mm.$ is the width of the central teeth and $w_{right/left_tooth} = 27\ mm.$ is the width linked to right and left teeth. So, the width of the TFLIM for the transversal flux, w_{trv} is equal to 51 mm.

$$w_{trv} = {w_{central_tooth}}/{2} + w_{right/left_tooth} \tag{66}$$

Case b) Analysis of Longitudinal Flux: Equation (67) defines the longitudinal reactance X_{long} [Ω] as a relation between the induced voltage that is originated by the longitudinal magnetic flux, $E_{long}[V]$ and the electric current consumed to create the longitudinal magnetic flux $I_{\emptyset_\text{long}}[A]$.

$$X_{long} = {E_{ind_{long}}}/{I_{\emptyset_{long}}} \begin{cases} E_{ind_{long}} = \sqrt{2} \cdot \pi \cdot N_P \cdot f \cdot K_{w1} \cdot B^y_{\delta_max} \\ \qquad \cdot \left({L_{long}}/{2 \cdot p}\right) \cdot w_{long} \\ I_{\emptyset_{long}} = \cdot B^y_{\delta_max} \cdot \pi \cdot \delta_{mec} / 6 \cdot \sqrt{2} \\ \qquad \cdot \mu_O \cdot K_{w1} \cdot N_P \end{cases} \tag{67}$$

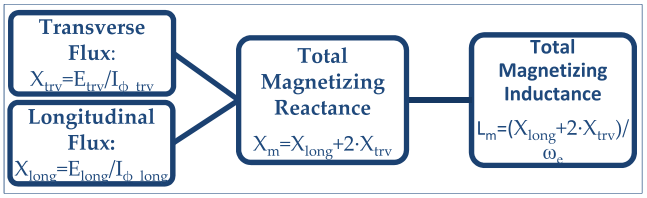

FIGURE 16. Process for estimation magnetizing inductance per phase.

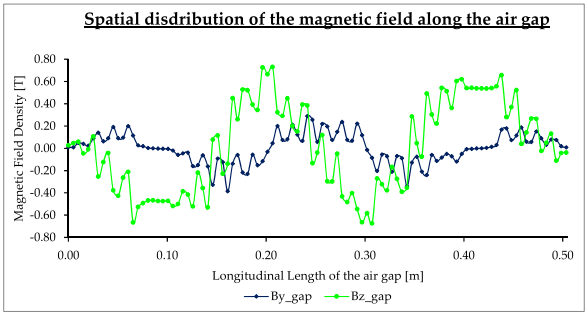

FIGURE 17. Field magnetic density along the air gap of the TFLIM.

$L_{long} = 400$ mm. and $w_{long} = 48$ mm. (the width of the central teeth). L_m is calculated by Eq. (68):

$$L_m = \left[\underbrace{\left(E_{ind_long}/I_{\emptyset_long}\right)}_{L_{m_long}} + \underbrace{2\cdot\left(E_{ind_trv}/I_{\emptyset_trv}\right)}_{L_{m_trv}} \right] \cdot 1/\left(\omega_e\right) \tag{68}$$

Fig. 16 shows the process followed to estimate the magnetizing inductance per phase where both magnetic fluxes, transverse and longitudinal, are considered. It is a useful method using FEM-3D to check the values obtained by indirect tests.

The TFLIM can be modelled as an array of harmonics with various pole pitches. Only the fundamental space harmonic ($\nu = 1$) corresponds to the magnetizing reactance. Thus, the sum of reactances for higher spaces harmonics $\nu > 1$ contributes to the leakage reactance [3]. In our work, we analyse the frequency spectrum associated to magnetic field density waves to select the fundamental harmonic needed to estimate the magnetizing inductance. Then, the following approximations are made (Eqs. (69) and (70)):

$$B_\delta^z = B_{\delta\nu}^z\,(\nu = 1) + \sum_{\nu=2}^{n} B_{\delta\nu}^z \approx B_{\delta\nu}^z\,(\nu = 1) \tag{69}$$

$$B_\delta^y = B_{\delta\nu}^y\,(\nu = 1) + \sum_{\nu=2}^{n} B_{\delta\nu}^y \approx B_{\delta\nu}^y\,(\nu = 1) \tag{70}$$

Fig. 17 shows the spatial distribution of transversal and longitudinal magnetic field density along the mechanical air gap. Longitudinal magnetic field is greater than transversal magnetic field. Comparing the peak value of both waves a ratio between them $B_{\delta_max}^z/B_{\delta_max}^y \approx 2.57$ is obtained.

TABLE 14. Comparison between transversal and longitudinal parameters.

Estimation of L_m per phase from field magnetic density B_g							
Transversal Field Magnetic Density				Longitudinal Field Magnetic Density			
B_{gz_max} [T]		0.72		B_{gy_max} [T]		0.28	
A_{max_trv} [A·turn]	I_{Φ_trv} [A]	E_{ind_trv} [V]	L_{m_trv} [mH]	A_{max_long} [A·turn]	I_{Φ_long} [A]	E_{ind_long} [V]	L_{m_long} [mH]
2990.900	35.591	48.619	4.348	1163.100	13.841	17.795	4.092
Total Magnetizing Inductance L_m[mH]=L_{m_long}+2·L_{m_trv}=12.788							

TABLE 15. Comparison between transversal and longitudinal parameters using indirect test.

Analysis of magnetizing inductance per phase						
Magnetizing inductance from indirect tests						
$L_{m_i_IT}$ [mH]	Test 1	Test 2	Test 3	Test 4	Test 5	Test 6
	10.500	11.300	11.800	12.300	12.900	14.900
L_{m_M1} [mH]	12.283					
Magnetizing inductance from field magnetic density along the air gap						
L_{m_M2} [mH]	12.789					
L_{m_Final} [mH]						**12.536**

Transversal magnetic flux generates a higher voltage, so transversal inductance contributes to the total magnetizing inductance considerably.

Table 14 shows the values obtained by each magnetic flux separately and Table 15 compares the values of magnetizing inductances per phase obtained by indirect test and the values analysing the magnetic field density. A_{max}, $I_\emptyset$ and E_{ind} are considerably largerr when transversal magnetic flux operates. These results show the goodness of the magnetic circuit linked to each magnetic flux, so the longitudinal magnetic circuit can be optimized to increase the value of L_m. Longitudinal magnetic circuit is characterized by the absence of a longitudinal magnetic yoke to concatenate the longitudinal magnetic flux among the central teeth, so the leakage magnetic flux is very important in our TFLIM.

To determine the final magnetizing inductance, the values obtained from indirect test and the values obtained analysing the field magnetic density along the central air gap must be compared. The corresponding data are showed in Table 15. The average values between both methods will be considered by Eq. (71).

$$L_{m_{Final}} = \left(\left(\frac{\left(\sum_{i=1}^{6} L_{m_{iIT}} \right)}{6} \right) + L_{m_{M2}} \right) \Big/ 2 = \left(L_{m_{M1}} + L_{m_{M2}}\right)/2 \tag{71}$$

where $L_{m_i_IT}$[mH] is the magnetizing inductance obtained from each indirect test. When these values are known, it is computed its average value L_{m_M1}[mH]. L_{m_M2}[mH] is the

TABLE 16. Values of secondary parameters from equivalent circuit obtained by indirect tests.

Secondary parameters	Test 1	Test 2	Test 3	Test 4	Test 5	Test 6
L_r[mH]	35.200	39.600	41.400	43.400	45.800	52.000
L_{lr}[mH]	24.700	28.300	29.700	31.100	32.900	37.100
X_r[Ω]	11.058	12.441	13.006	13.635	14.388	16.336
X_{lr}[Ω]	7.760	8.891	9.331	9.770	10.336	11.655
R_r[mΩ]	131.900	117.300	127.600	139.500	153.900	86.300
Z_r[Ω]	13.509	15.291	16.007	16.774	17.716	20.068
X_r[Ω]/R_r[Ω]	83.839	106.059	101.929	97.738	93.492	189.296

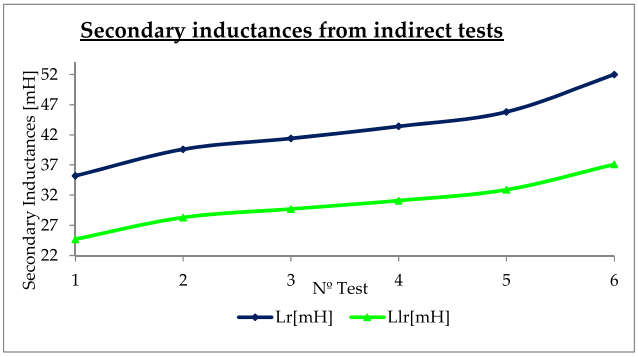

FIGURE 18. Secondary Inductances from indirect tests.

magnetizing inductance obtained from field magnetic induction and L_{m_Final}[mH] is the average value between both methods. The values of L_{m_M1} and L_{m_M2} are closed with a difference of 0.506 mH. Final magnetizing inductance is around 12.5 mH which corresponds to a magnetizing reactance around 3.92 Ω for a nominal frequency of 50 Hz according to Eq. (72).

$$\chi_{m_Final} = \omega_e \cdot L_{m_{Final}} \tag{72}$$

2) ANALYSIS OF SECONDARY PART PARAMETERS

This section presents results obtained to the parameters of the secondary part. Table 16 collects the inductances $\boldsymbol{L_r}$ and $\boldsymbol{L_{lr}}$, the reactances $\boldsymbol{X_r}$ and $\boldsymbol{X_{lr}}$, the secondary resistance $\boldsymbol{R_r}$ and the total impedance of the secondary part $\boldsymbol{Z_r}$.

Fig. 18 shows the behaviour of the main inductances. Both secondary leakage inductances and total secondary inductance increase with the number of simulated tests. The evaluation of leakage inductance, $\boldsymbol{L_{lr}}$, is very important in our TFLIM although only the central teeth contributes to the generation of a positive thrust force. Thus, in the aluminium layer only a part of the eddy currents induced generates a useful magnetic flux. Therefore, leakage flux in secondary part cannot be neglected and fluctuates between 24.7 mH and 37.1 mH.

Fig. 19 shows the reactance $\boldsymbol{X_{lr}}$. The leakage reactance varies between 7,7 Ω and 11.6 Ω. Then, using the magnetizing inductance, can be estimated the total inductance and reactance of the secondary part, $\boldsymbol{L_r}$ and $\boldsymbol{X_r}$ respectively. According to Figs. 18 and 19, this inductance varies between

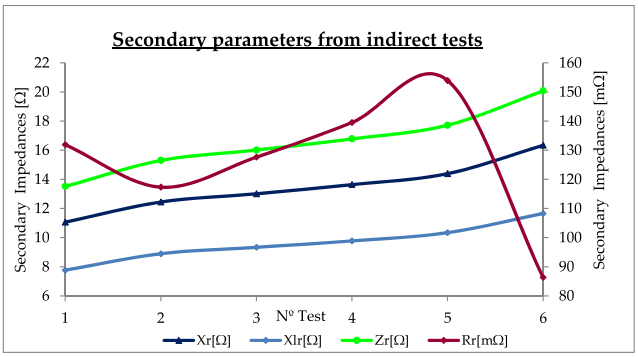

FIGURE 19. Secondary impedances and resistance from indirect tests.

35.2 mH and 52 mH and its equivalent reactance fluctuates between 11 Ω and 16.3 Ω.

Secondary resistance $\boldsymbol{R_r}$ is also computed. This parameter decreases in opposition to reactance. Fig. 19 shows the variation of it in the different simulation tests. Starting with a value around 132 mΩ for test 1 and reaching a final value around 86.3 mΩ in test 6. According to our system of equations all $\boldsymbol{R_r}$ develop a positive thrust force along the direction of the movement. The total impedance of the secondary is dominated by the imaginary component given by $\boldsymbol{X_r}$. Analysing $\boldsymbol{Z_r}$, the ratio between imaginary and real part X_r/R_r is calculated. Additionally, it can be proved that $\boldsymbol{X_r}$>$\boldsymbol{R_r}$ as shown in Table 16. The value of $\boldsymbol{Z_r}$ is very close to the reactance values and fluctuates between 13.5 Ω and 20.8 Ω as shown in Fig. 19.

a: SECONDARY PART ESTIMATION FROM 2-D FIELD THEORY

To check the results of the indirect tests, a classical method based on 2-D field theory is applied. Using equations from this method, we are going to show the high capabilities from FEM-3D simulations. These tools allow consider all phenomena involved in a TFLIM. With classical methods, it is not possible. Classical methods can only consider LIM operating under longitudinal magnetic flux along a 2-D plane, which can be a first approximation to our solutions derived from simulations in FEM-3D tools.

Therefore, the secondary impedance can be estimated following these five steps:

1. Computation of **Russell and Norsworthy coefficient** to calculate the edge effect, K_{RNv}. This phenomenon is produced by non-effective path originated by the induced eddy currents in the secondary part, and it only occurs in flat LIM [4]. Edge effect produces non-aided consequences due to the presence of components of eddy current which does not contribute to the generation of thrust force along the direction of the travelling magnetic field. Mainly, non-uniform distribution of magnetic density in the air gap and lateral forces generation are the main inconvenient associated to edge effect. To estimate it, the edge effect is included into dimensionless parameters

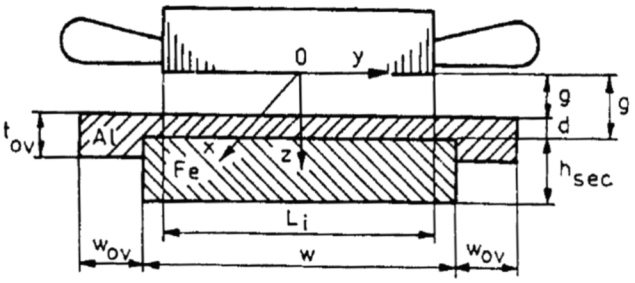

FIGURE 20. Schematic representation of dimensions from secondary part of a LIM [4].

$K_{RN\upsilon}$. This decreases the conductivity to the secondary layers. In our work it is assumed that the electric conductivity of the steel layer is zero, so edge effect appears exclusively within the aluminium layer.

Eqs. (73) and (74), as shown at the bottom of the next page, calculate the dimensionless parameter $\boldsymbol{K_{RN\upsilon}}$ and the correction in the aluminium electrical conductivity, $\boldsymbol{\sigma'_{Al}}[S \cdot m^{-1}]$ respectively. $\boldsymbol{\omega}[rad/s]$ is the angular frequency; $\boldsymbol{\beta_\upsilon}[rad/m]$ is a parameter derived from Helmholtz's equation that include the propagation of electromagnetic waves in conductive layers (see Eq. (76)), as shown at the bottom of the next page, where υ is the harmonic number and p is the number of pair of poles). $\boldsymbol{k_t}$, is defined by Eq. (75), as shown at the bottom of the next page, and it is a dimensionless parameter that includes the effect of the different thickness of the two layers in the secondary part. In this equation the parameters $\boldsymbol{d}[mm]$ and $\boldsymbol{t_{ov}}[mm]$ are the dimensions shown in Fig. 20. In our TFLIM the value of d is equal to t_{ov}; $\boldsymbol{w_{ov}}$ $[mm]$ is the difference of width between the aluminium and steel layer shown in Fig. 20.

2. Computation of $\boldsymbol{K_{trv}}$ and $\boldsymbol{K_{trv}}$:
   - $\boldsymbol{K_{trv}}$: It is defined by Eq. (78), as shown at the bottom of the next page, and it is the turns ratio reducing the secondary impedance to the primary system. m_1 is the number of phases, N_1 is the number of turns per phase, K_{w1} is the winding factor. According to [3] it is possible to estimate this parameter using $N_2 = 0.5$ and the winding factor for the secondary part $K_{w2} = 1$. Additionally, the number of phases of the secondary part can be calculated by Eq. (77), as shown at the bottom of the next page.
   - $\boldsymbol{K_{zv}}$: it represents the edge effect phenomenon within the steel layer (see Eq. (79)). We assume that it will increase the secondary impedance in solid ferromagnetic layer. In general, the solid ferromagnetic core conducts magnetic flux and eddy current induced, so although in our TFLIM the electric conductivity in this layer is zero, we need to consider its influence due to the magnetic permeability.

$$K_{zv} = 1 - {}^{g}\!/_{\upsilon \cdot L_i} + \left({}^{2 \cdot \tau_p}\!/_{\upsilon \cdot \pi \cdot \omega}\right) \cdot \left(1 - e^{-\left({}^{\upsilon \cdot \pi \cdot \omega}\!/_{2 \cdot L_i}\right)}\right) \quad (79)$$

TABLE 17. TFLIM secondary parameters from 2D-field theory.

Secondary parameters according to 2D Field Theory								
Geometric Parameters							Electrical properties	
K_{w1}	w_{ov}[mm]	t [mm]	d [mm]	h_{sec} [mm]	L_i[mm]	K_t	σ_{Al} [S/m]	σ_{Fe}[S/m]
0.6773	0.0525	0.01	0.01	0.025	0.3	1	0	3.73E+07
Russell and Norsworthy coefficient							$K_{RN\upsilon}$	β_υ	σ'_{Al} [S/m]
							0.99976	15.7080	3.7291E+07
Dimensionless Parameters							K_τ	K_{trv}
							0.98374	5328.669
Attenuation Factor							k_{Al}	k_{Fe}
							15.7780	15.7080
Secondary Part Paremeters								
Z_{Al}[Ω]		Z_{Fe}[Ω]		Z_2[Ω]			R_2[mΩ]	X_2[Ω]
0.2344 + j·1.2449		0 +j·1.3221E+03		0.2340 +j·1.2437			234	1.2437

3. Computation of $\boldsymbol{k_{Al}}$ and $\boldsymbol{k_{Fe}}$: they are the attenuation factor of the fundamental space harmonic in the aluminium and the steel layer, respectively. Equations (80) and (81) calculate both coefficients.

$$k_{Al} = \sqrt{j \cdot s \cdot \mu_0 \cdot \sigma'_{Al} + \left({}^{\pi}\!/_{\tau_P}\right)^2} \quad (80)$$

$$k_{Fe} = \sqrt{j \cdot s \cdot \mu_{Fe} \cdot \sigma_{Fe} + \left({}^{\pi}\!/_{\tau_P}\right)^2} \quad (81)$$

4. Computation of $\boldsymbol{Z'_{\upsilon Al}(s_\upsilon)}$ and $\boldsymbol{Z'_{\upsilon Fe}(s_\upsilon)}$: they are the impedance of each layer from secondary part, that is, the impedance of aluminium and the steel layer respectively. They present a direct dependence of the harmonic number s_υ. See Eqs. (82) and (83).

$$Z'_{\upsilon Al}(s_\upsilon) = \left(j \cdot s_\upsilon \cdot \omega \cdot \mu_0 \cdot K_{trv} \cdot \upsilon \cdot L_i\right) \Big/ \left(k_{\upsilon Al} \cdot tanh\left(k_{\upsilon Al} \cdot d\right) \cdot \tau_p\right) \quad (82)$$

$$Z'_{\upsilon Fe}(s_\upsilon) = \left(j \cdot s_\upsilon \cdot \omega \cdot \mu_{Fe} \cdot K_{trv} \cdot K_{z\upsilon} \cdot \upsilon \cdot L_i\right) \Big/ \left(k_{\upsilon Fe} \cdot tanh\left(k_{\upsilon AFe} \cdot h_{sec}\right) \cdot \tau_p\right) \quad (83)$$

5. The value of the secondary impedance $\boldsymbol{Z'_{2\upsilon}}$ of the secondary part composed by a double layer reaction rail is calculated by Eq. (84).

$$Z'_{2\upsilon} = \left(\left(Z'_{\upsilon Al}(s_\upsilon) \cdot Z'_{\upsilon Fe}(s_\upsilon)\right) \Big/ \left(Z'_{\upsilon Al}(s_\upsilon) + Z'_{\upsilon Fe}(s_\upsilon)\right)\right) {}^{1}\!/_{s_\upsilon} = {}^{R'_{2\upsilon}(s_\upsilon)}\!/_{s_\upsilon} + j \cdot \left({}^{X'_{2\upsilon}(s_\upsilon)}\!/_{s_\upsilon}\right) \quad (84)$$

Table 17 shows the results applying 2D Field Theory. Our analysis considers $\upsilon = 1$ and standstill condition. It can be checked that transversal effect is not relevant with Russell and Norsworthy coefficient are close to one, so the electrical conductivity is not very influenced. With this method we can estimate the impedance of each layer considering the same properties used with FEM-3D simulations. Then, the impedance of iron layer is higher than aluminium layer. In fact, imaginary part in ferromagnetic layer is considerably higher than the non-ferromagnetic layer like aluminium.

Additionally, it is important to compare the results obtained by indirect test with FEM-3D and using 2D Field Theory. So, if we analyse the real part of the secondary impedance, we can establishe that with FEM-3D the values of R_r oscillate between 131.9 mΩ and 86.3 mΩ and with 2D Field Theory the value is close to 240 mΩ. Nevertheless, imaginary part X_r presents a huge divergence between both methods. Using indirect tests, it reaches a value between 11.058 Ω and 16.336 Ω approximately and with 2D Field Theory its value is smaller, around 1.2 Ω. This difference implies that 2D Field Theory is not suitable when we analyse TFLIM, whose internal configuration by three internal motors where the central and lateral teeth contribute to the generation of the net thrust force, is not considered in 2D Field Theory. The eddy currents induced above each tooth are different in each case, so the lateral and central teeth will produce a particular leakage flux in each case with a singular transversal effect. All these limitations suppose that 3D simulations are the correct method to estimate the EC parameters in a TFLIM.

VI. GOODNESS FACTOR APPLIED TO TFLIM

In this section the TFLIM design is evaluated using a dimensionless KPI (Key Performance Indicator) G. It is estimated by Eq. (85) and allows us to evaluate the electromagnetic conversion as the ratio between magnetizing reactance and secondary resistance. According to [22] it is recommendable that $\mathcal{G} > 1$ to assure that a LIM operates correctly, although this parameter will not consider the leakage reactance.

$$\mathcal{G} = {}^{X_m}/_{R_r} \tag{85}$$

Table 18 shows interesting results because it includes the values of goodness factor taking the values of the indirect tests. In tests 1 to 5 the values of $\mathcal{G}$ are very similar, so an average value of $\mathcal{G}$ around 27.7 can be used. However, in test 6 the goodness factor is increased considerably to 54.3. When values of magnetizing reactance and secondary resistance obtained by theoretical methods have been used, the goodness factor decreases with respect to the average value from 3D-FEM, so its value is around 16.8. Finally, Fig. 21 represents the behaviour of TFLIM goodness factor obtained with the values of the indirect tests.

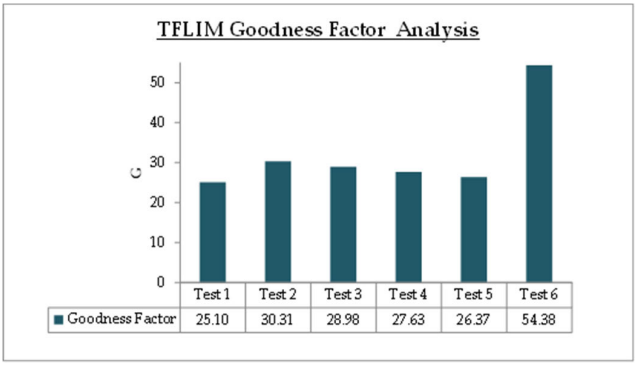

FIGURE 21. TFLIM goodness factor from indirect tests.

TABLE 18. Comparison of TFLIM goodness factor.

TFLIM Goodness Factor Analysis					
Method A: Indirect Test					
Test 1	**Test 2**	**Test 3**	**Test 4**	**Test 5**	**Test 6**
25.10	30.31	28.98	27.63	26.37	54.38
Method B: Theoretical method					
Magnetizing Reactance [Ω]		Secondary Resistance [Ω]		Goodness Factor	
3.938		0.234		16.830	

VII. CONCLUSION

This paper simulates with FEM-3D the indirect tests that are commonly used in electrical laboratories to identify all the parameters belonging to an EC model. Six no load and standstill tests are carried out with simulations in transitory state. This paper proposes as a novelty a system of equations to determine the main parameters from the EC induction motor adapted to the particularities of a LIM. The proposed system of equations includes the coefficient β that implies a relationship between the magnetizing inductance and the secondary inductance. β is set to 0.3 to obtain a convergence solution.

An important novelty of this paper is to include in the model an anti-thrust force that appears due to the longitudinal end-effect. This effect cannot be neglected in a TFLIM, so the estimation of the EC parameters must consider it.

$$K_{RNv} = 1 - \left({}^{tanh\left(\beta_v \cdot {}^{\omega}/_{2}\right)}/_{\left(\left(\beta_v \cdot {}^{\omega}/_{2}\right) \cdot \left(1 + K_t \cdot tanh\left(\beta_v \cdot {}^{\omega}/_{2}\right) \cdot tanh\left(\beta_v \cdot w_o\right)\right)\right)} \right) \leq 1 \tag{73}$$

$$\sigma'_{Al} = K_{RNv} \cdot \sigma_{Al} \tag{74}$$

$$k_t = 1 + 1.3 \cdot {}^{(t_o - d)}/_{d} \geq 1 \tag{75}$$

$$\beta_v = v \cdot \left({}^{\pi}/_{2 \cdot p} \right) \tag{76}$$

$$m_2 = 2 \cdot v \cdot p \tag{77}$$

$$K_{trv} = \underbrace{m_1 \cdot (N_1 \cdot k_{w1})^2 / m_2 \cdot (N_2 \cdot k_{w2})^2 = 2 \cdot m_1 \cdot (N_1 \cdot K_{w1})^2 / v \cdot p}_{N_2 = 0.5, K_{w2} = 1 \text{ and } m_2 = 2 \cdot v \cdot p} \tag{78}$$

For example, in case of test 1 the relationship between net thrust force and anti-thrust force is about 3.1. For some range of frequencies, some EC parameters have been calculated mathematically. In these cases, linear regression curves have been applied to estimate them, simulations with FEM-3D not being necessary.

Magnetizing inductance in the indirect tests varies between 10.5 mH and 14.9 mH. These values are similar to the magnetizing inductance obtained when the experience begins with the analysis of the magnetic field density along the air gap. An imaginary path that crosses the central teeth calculates this density. Therefore, the magnetizing inductance must be estimated by calculating the transversal and longitudinal magnetizing inductances. The longitudinal is around 0.72 mH while the transversal reaches 0.28 mH. Both inductances give a final value of 12.78 mH, which is between the maximum and minimum obtained from the indirect tests. Both methods give the same results, so we can conclude that the use of FEM-3D simulations, the proposed system of equations and the estimation of the magnetizing inductance are correct.

This paper also analyses the primary part of the motor considering three specific effects that occurs in LIMs, skin effect, fringing effect, and effective air gap. The skin effect due to a double layer winding located in an E-shaped armature has a great influence, because the primary resistance per phase is multiplied by 4.2 times respect to the DC resistance value. We have also calculated the effect of a particular primary part structure that includes open slots, resulting in an increase in the effective air gap. The fringing effect is not relevant in our TFLIM, so it can be omitted in the EC.

Two different methods has been established to analyse the secondary part. The limitations of 2-D field theory on our TFLIM are shown, and how our proposed method is better. With indirect tests we have determined a secondary part reactance between 11.1Ω and 16.3 Ω, however with 2D Field Theory it is around 1.2 Ω. On the contrary, there is a greater convergence between secondary part reactance than imaginary part. For example, in test 6 the reactance reaches 131.3 mΩ and using 2D Field Theory 234 mΩ. Therefore, we can conclude that the classical 2D field theory for estimation of the EC parameters is not adequate, but it can help us to give a first approximation. Finally, a goodness factor is also calculated to particularize a TFLIM. To this end, some changes in the geometrical dimensions are included. In our TFLIM this KPI can be very useful to assess the effects on the EC parameters.

Simulations of indirect tests carried out with FEM-3D in transitory conditions are a great advantage to avoid unnecessary experiments in real electrical laboratories. The main limitation of using FEM-3D is the assumption that the electrical conductivity of the secondary steel layer is equal to 0 S/m. To simulate this effect, the introduction of a non-linear BH curve is required, which implies a great computation effort. Each proposed test will need sufficient time for the equations solver to converge to the correct solutions. The proposed system of equations and the linear regressions represent an easy method to a first estimation of the EC parameters. Future works include incorporating this model into a control system to analyse its performance when power electronics are applied in the implementation of a vector control technique in a TFLIM.

REFERENCES

[1] E. R. Laithwaite, *A History of Linear Electric Motors*. New York, NY, USA: Macmillan, 1987.
[2] Z. Liu, Z. Long, and X. Li, *Maglev Trains: Key Underlying Technologies*. New York, NY, USA: Springer, 2015.
[3] S. N. Nasar and I. Boldea, *Linear Electric Actuators and Generators*. Cambridge, U.K.: Cambridge Univ. Press, 1997.
[4] J. F. Gieras, *Linear Induction Drives*. Oxford, U.K.: Clarendon, 1994.
[5] S. N. Nasar and I. Boldea, *Linear Motion Electric Machines*. Hoboken, NJ, USA: Wiley, 1976.
[6] N. Bianchi, *Electrical Machine Analysis Using Finite Elements*. Boca Raton, FL, USA: CRC Press, 2005.
[7] M. Rosu, P. Zhou, D. Lin, D. Ionel, M. Popescu, F. Blaabjerg, V. Rallabandi, and D. Staton, *Multiphysics Simulation by Design for Electrical Machines, Power Electronics and Drives*. Piscataway, NJ, USA: IEEE Press, 2018.
[8] L. Papini and C. Gerada, "Sensitivity analysis of rotor parameters in solid rotor induction machine," in *Proc. IEEE Int. Electr. Mach. Drives Conf. (IEMDC)*, May 2017, pp. 1–6.
[9] G. Kang, J. Kim, and K. Nam, "Parameter estimation scheme for low-speed linear induction motors having different leakage inductances," *IEEE Transactions on Industrial Electronics*, vol. 50, no. 4, pp. 708–716, Aug. 2003, doi: 10.1109/TIE.2003.814864.
[10] G. Kang, J. Kim, and K. Nam, "Parameter estimation of a linear induction motor with PWM inverter," in *Proc. 27th Annu. Conf. IEEE Ind. Electron. Soc. (IECON)*, vol. 2, Nov./Dec. 2001, pp. 1321–1326, doi: 10.1109/IECON.2001.975973.
[11] C. Yang and J. Yang, "Off-line parameter identification of linear induction motor based on PWM inverter," in *Proc. 5th Int. Conf. Control, Autom. Robot. (ICCAR)*, Apr. 2019, pp. 477–481, doi: 10.1109/ICCAR.2019.8813724.
[12] G. Lv, T. Zhou, D. Zeng, and Z. Liu, "Design of ladder-slit secondaries and performance improvement of linear induction motors for urban rail transit," *IEEE Trans. Ind. Electron.*, vol. 65, no. 2, pp. 1187–1195, Feb. 2018, doi: 10.1109/TIE.2017.2726967.
[13] G. Lv, T. Zhou, and D. Zeng, "Quasi-3D analytic method of the single-sided linear induction motor with the ladder secondary," *IEEE Trans. Ind. Electron.*, vol. 68, no. 12, pp. 11817–11825, Dec. 2021, doi: 10.1109/TIE.2020.3047059.
[14] D. Zeng, G. Lv, and T. Zhou, "Equivalent circuits for single-sided linear induction motors with asymmetric cap secondary for linear transit," *IEEE Trans. Energy Convers.*, vol. 33, no. 4, pp. 1729–1738, Dec. 2018, doi: 10.1109/TEC.2018.2840057.
[15] S. G. Lee, H.-W. Lee, S.-H. Ham, C.-S. Jin, H.-J. Park, and J. Lee, "Influence of the construction of secondary reaction plate on the transverse edge effect in linear induction motor," *IEEE Trans. Magn.*, vol. 45, no. 6, pp. 2815–2818, Jun. 2009, doi: 10.1109/TMAG.2009.2018669.
[16] V. A. Solomin, A. V. Solomin, and L. L. Zamshina, "Mathematical modeling of currents in secondary element of linear induction motor with transverse magnetic flux for magnetic-levitation transport," in *Proc. Int. Conf. Ind. Eng., Appl. Manuf. (ICIEAM)*, Mar. 2019, pp. 1–6, doi: 10.1109/ICIEAM.2019.8742920.
[17] A. V. Solomin, V. A. Solomin, and N. A. Trubitsina, "Approaches to modeling current distribution in winding of linear induction motor with transverse magnetic flux," in *Proc. Int. Ural Conf. Electr. Power Eng. (UralCon)*, Oct. 2019, pp. 266–270, doi: 10.1109/URALCON.2019.8877690.
[18] J. Y. Lee, J. P. Hong, J. H. Chang, and D. H. Kang, "Computation of inductance and static thrust of a permanent-magnet-type transverse flux linear motor," *IEEE Trans. Ind. Appl.*, vol. 42, no. 2, pp. 487–494, Mar./Apr. 2006, doi: 10.1109/TIA.2005.863900.
[19] G. Lv, D. Zeng, and T. Zhou, "An advanced equivalent circuit model for linear induction motors," *IEEE Trans. Ind. Electron.*, vol. 65, no. 9, pp. 7495–7503, Sep. 2018, doi: 10.1109/TIE.2018.2807366.

[20] R. M. Pai, I. Boldea, and S. A. Nasar, "A complete equivalent circuit of a linear induction motor with sheet secondary," *IEEE Trans. Magn.*, vol. MAG-24, no. 1, pp. 639–654, Jan. 1988, doi: 10.1109/20.43997.
[21] A. Zare-Bazghaleh, M. R. Naghashan, and A. Khodadoost, "Derivation of equivalent circuit parameters for single-sided linear induction motors," *IEEE Trans. Plasma Sci.*, vol. 43, no. 10, pp. 3637–3644, Oct. 2015, doi: 10.1109/TPS.2015.2474746.
[22] E. R. Laithwaite, *Induction Machines for Special Purposes*. New York, NY, USA: Chemical Publishing Company, 1966.
[23] J. J. M. Rivas, "Estudio de la interacción magneto-eléctrica en el entrehierro de los motores lineales de inducción de flujo transversal. Aplicación al diseño de un prototipo para tracción ferroviaria de tren monoviga," Ph.D. thesis, Departamento de Ingeniería Eléctrica, Universidad Politécnica de Madrid, Madrid, Spain, 2003.
[24] J. A. Dominguez, N. Duro, and E. Gaudioso, "A 3-D simulation of a single-sided linear induction motor with transverse and longitudinal magnetic flux," *Appl. Sci.*, vol. 10, no. 19, p. 7704, Oct. 2020.
[25] J. Pyrhonen, T. Jokinen, and V. Hrabovcova, *Design of Rotating Electrical Machines*. Hoboken, NJ, USA: Wiley, 2014.
[26] J. F. Gieras, *Electrical Machines: Fundamentals of Electromechanical Energy Conversion*. Boca Raton, FL, USA: CRC Press, 2017.
[27] N. Toro, Y. G. Gomez, F. Hoyos, and E. Sanchez, "Parameter estimation of linear induction motor labvolt 8228–02," in *Proc. Congreso Anual, Asociación de México de Control Automático*, 2011, pp. 5–7.
[28] J. Duncan, "Linear induction motor—Equivalent circuit model," *IEE Proc. B, Electr. Power Appl.*, vol. 130, no. 1, pp. 51–57, Jan. 1983.
[29] C. Steven, R. Chapra, and P. Canale, *Métodos Numéricos Para Ingenieros*. New York, NY, USA: McGraw-Hill, 2015.
[30] R. Johnson and P. Kuby, *Estadística Elemental: Lo Esencial*. Boston, MA, USA: Cengage Learning, 1999.
[31] M. F. Triola, *Estadística*. London, U.K.: Pearson, 2004.
[32] I. Boldea, *Linear Electrical Machines, Drives, and Maglevs Handbook*. Boca Raton, FL, USA: CRC Press, 2013.

JUAN ANTONIO DOMÍNGUEZ HERNÁNDEZ was born in Madrid, Spain, in 1983. He received the B.E. degree in electrical engineering from the University Carlos III of Madrid, Getafe, in 2013. He is currently pursuing the Ph.D. degree in system and control engineering with the Department of Computer Science and Automation, Universidad Nacional de Educación a Distancia (UNED). He has collaborated in the design of several linear electrical machinery with finite element tools, both synchronous motors and asynchronous devices.

NATIVIDAD DURO CARRALERO received the degree in physical sciences from the Universidad Complutense de Madrid and the Ph.D. degree in sciences from the Universidad Nacional de Educación a Distancia (UNED). She is currently an Assistant Professor with the Department of Computer Science and Automation, UNED. Her main research interests include control and modeling of processes, design of new systems oriented to education, data mining, signal processing, and big data.

ELENA GAUDIOSO VÁZQUEZ received the B.Sc. degree in mathematics from the Universidad Complutense de Madrid, Madrid, Spain, in 1996, and the Ph.D. degree in sciences from the Universidad Nacional de Educación a Distancia (UNED), Madrid, in 2003. She is currently an Associate Professor with the Department of Artificial Intelligence, UNED. She has authored or coauthored more than 30 papers about educational and adaptive systems in international journals and conferences. Her research interests include educational systems, recommender systems, adaptive systems, and machine learning.